学位論文(要約)

Development and application of turbulence estimation using a fast-response thermistor attached to a CTD frame

(CTD フレーム搭載型高速水温計を用いた乱流見積もり手法の開発と適用)

平成 29 年 12 月博士（理学）申請

東京大学大学院理学系研究科

地球惑星科学専攻

後藤恭敬

Doctoral Dissertation

Development and application of turbulence estimation using a fast-response thermistor attached to a CTD frame

by

Yasutaka Goto

Department of Earth and Planetary Science

Graduate School of Science

The University of Tokyo

December 2017

Abstract

Turbulence observations have been limited because of the difficulty in microstructure measurements. In order to efficiently obtain much more turbulence data down to the ocean floor without spending extra ship-time, we propose a new method, a microstructure profiler attached to a CTD-frame (Conductivity-Temperature-Depth). Since microstructure measurements of velocity shear are sensitive and fragile to vibration of instruments, measurements have been performed with free-fall or free-rise instruments whose vibrations to generate noise are minimized. Since the profiler attached to the CTD-frame cannot suppress vibrations, we choose fast-response thermistors to measure micro-temperature fields which is much less sensitive to the vibrations than velocity fields. However, since turbulence estimation from thermistors have not been common due to their insufficient temporal response, assessment of availability is necessary. In this thesis, the method of turbulence estimation using fast-response thermistors attached to CTD frames is developed by the following steps.

First, estimation of turbulence intensity using fast-response thermistors is assessed by comparing the energy dissipation rate ε_T from FP07 (Fastip Probe model 07) thermistors with ε_S from shear probes, both of which are attached to a free-fall microstructure profiler with the fall rate of 0.6 - 0.7 ms^{-1} in Chapter 2. ε_T tends to be less than ε_S for increasing ε_S in the case without any corrections to temperature gradient spectra. The high frequency part of temperature gradient spectra from the thermistors is known to attenuate as single- or double-pole low-pass filter functions (Lueck et al., 1977; Gregg and Meager 1986). However, fast-response thermistors have not been used due to the lack of availability assessment. In the present study, multiplying the reciprocal of the functions

with the time constant of 7 milli-second (single-pole) or 3 milli-second (double-pole) to the temperature gradient spectra is shown to be effective to resume the spectra. ε_T is shown to be consistent with ε_S within a factor of 3 in the wide range of $10^{-10} < \varepsilon_S < 10^{-7}$ Wkg^{-1}. From the result, fast-response thermistor measurement is concluded to be practical if temperature gradient spectra are corrected.

Second in Chapter 3, availability of thermistors is assessed in the case where they are attached to CTD frames which are connected with ship through steel cable and ship motion and vibration may directly affect microstructure measurements. Turbulence intensities estimated from fast-response thermistors are compared between CTD-attached and free-fall microstructure profilers, conducted at the same location within about 2 hours. The agreement is shown to be generally good, but anomalously overestimated data, deviating from a log-normal distribution, appear sporadically in the CTD-attached method. These overestimated outliers are evident as spiky patches in the raw temperature gradient profiles. It is shown that the outliers often occur when the fall rate of the CTD frame, W (in ms^{-1}), is small, and its standard deviation, W_{sd}, is large. These overestimated outliers are shown to be efficiently removed by rejecting data with the criteria of $W_{sd} > 0.2W$-0.06, where W and W_{sd} are computed for a 1 s interval. After the data screening, thermal and energy dissipation, χ and ε, from CTD-attached and free-fall profilers are consistent within a factor of 3 in the ranges of $10^{-10} < \chi < 10^{-7}$ °C^{2}s^{-1} and $10^{-10} < \varepsilon < 10^{-8}$ Wkg^{-1} for 50 m depth-averaged data.

Basin-scale distribution of turbulence intensity in the deep northwestern Pacific is revealed from 438 observations in Chapter 4, by rejecting data at which $W_{sd} > 0.2W$-0.06 as in Chapter 3 and W is local minimum. The method is also validated by comparing with previous fine-scale O(10~100m) methods. Turbulence is intensified over rough topography at around seamounts and ridges where internal tides are generated. Turbulence intensity represented by energy dissipation rate ε_{T} depends on internal tide energy and squared buoyancy frequency N^2 ($\propto$ vertical density gradient) through comparing with $\varepsilon_{\mathrm{MODEL}}$ used in a previous ocean general circulation model (OGCM) which reproduced deep Pacific water-masses fields (Oka and Niwa, 2013). $\varepsilon_{\mathrm{MODEL}}$ is shown to be much larger than ε_{T} by more than 10 times, although spatial variability is correlated between ε_{T} and $\varepsilon_{\mathrm{MODEL}}$. This difference is relaxed to be within a factor of 3 by changing the vertical structure of $\varepsilon_{\mathrm{MODEL}}$ away from internal tide generation sites to be proportional to N^2, and by reducing the background constant vertical diffusivity to be at 10^{-7} m^2s^{-1}, 1/100 times of the previous model. By conducting widespread observations of CTD-attached thermistors with higher spatial and temporal resolutions, more realistic OGCM with better diapycnal diffusivity distribution will be developed in future.

Contents

List of Figures

Fig. 2.4. Same as Fig. 2.2a but for the data after applying (a) the single-pole and (b) the double-pole corrections to spectra with the time constant of τ_0 = 7 msec and τ_0 = 3 msec, respectively. The yellow dots with lines are the geometric mean of ε_T and ε_S in the ranges of $10^{-(i+1)} < \varepsilon_S < 10^{-i}$ for i = 6, 7, …10.

Fig. 2.5. Dependence of the ε_T-ε_S relation on the time constant τ_0 of individual FP07 thermistors. The plus marks with lines are the geometric means of ε_T in the ranges of $10^{-(i+1)} < \varepsilon_S < 10^{-i}$ (i = 7, 8, 9). (a) single-pole correction with τ_0 = 7 msec and (b) double-pole correction with τ_0 = 3 msec. (c, d) For the cases where optimally computed τ_0 by minimizing $\log_{10}|\varepsilon_T/\varepsilon_S|$ are used for (c) single- and (d) double-pole corrections.

Fig. 2.6. Dependence of the ratio $\log_{10}(\varepsilon_T/\varepsilon_S)$ on the frequency at the peak of the Kraichnan fitted spectra, f_p, which is corrected by (a) the single-pole and (b) the double-pole frequency response functions with the time constant of τ_0 = (a) 4, 7, 10 and (b) 2, 3, 4 msec. Colored curves represent 101-point running means as in Fig. 2.3.

Fig. 2.7. Dependence of $\log_{10}(\varepsilon_T/\varepsilon_S)$ on the buoyancy Reynolds number $I = \varepsilon_S/(\nu N^2)$. Dots denote the data satisfying $\varepsilon_S > 3\times10^{-10}$ Wkg^{-1} from seven probes. Temperature spectra are corrected by the double-pole functions with the time constant of 3 msec. The thick red curve represents the 21-points running mean of the dots. The thin red curve represents the 21-point running mean data in the case of without correction. Vertical solid lines indicate I = 20 and 100 between which ε_S are reliably estimated in spite of the violation of isotropic turbulence assumption.

Fig. 2.8. Dependence of $\log_{10}(K_T/\kappa)$ (the ratio of the total thermal diffusivity divided by the molecular thermal diffusivity) on the buoyancy Reynolds number *I*. Data of $\varepsilon_T < 10^{-10}$ (weak turbulence) and -45° < *Tu* < 45° (in this Turner angle *Tu* range, no double diffusion occurs) is shown from the seven probes. Blue (red) dots represent data using ε_S (ε_T) to calculate *I*. The solid line is $y = 0.2Prx$ over $7 < I < 100$, where Prandl number $Pr = \nu/\kappa$ is set at the constant value of 12.

Fig. 2.9. Examples of (a) velocity shear spectra and (b) temperature gradient spectra in the weak turbulence range of $\varepsilon_S < 10^{-10}$ and $\varepsilon_T < 10^{-12}$ $\mathrm{Wkg^{-1}}$ from the data in Fig. 2.2. Black curves are observed spectra. All the temperature spectra passed the criterion tests of PF14. Cyan and magenta are the universal Nasmyth and Kraichnan spectra, respectively for $\varepsilon, \chi = 10^{-12}, 10^{-11}, 10^{-10}$. Blue and red curves denote the spectra with the minimum (a) ε_S and (b) χ for S1, S2, T1, and T2 sensors.

Fig. A1. Scatter plots showing the difference between ε_{S1} and ε_{S2}, where they are from concurrently measured two shear probes S1 and S2. Data with poorly fitted spectra to the Nasmyth spectrum is not used.

Fig. 3.1. (a) Micro Rider 6000 attached to the CTD-frame during the cruise of KS-15-5 and (b) AFP07 during the cruise of KH-16-3. The probes of FP07 thermistors were set close to the bottom of the frame. ©American Meteorological Society. Used with permission.

Fig. 3.2. Positions of the 72 stations of the CTD-attached (circles) fast response thermistor measurements (Micro Rider 6000 or AFP07) where free-fall measurements using the vertical microstructure profiler 2000 (VMP) were also performed within 2 hours from the CTD casts. Triangles denote the stations where the repeat casts of the free-fall VMP were performed within 2 hours to examine the temporal variability in the appendix. ©American Meteorological Society. Used with permission.

Fig. 3.3. Examples of observed (black) and fitted (red) Kraichnan temperature gradient spectra of free-fall VMP (a - d) and CTD-attached MR (e, f) from the 1-sec-bins. (a) and (b) are examples with noise spectra (light-blue curve) and 1st order power low fit with a (a/b) positive/negative slope of the straight line (blue line). (c) and (e) are examples of well fitted spectra with low maximum absolute deviation MAD (< 0.4) and likelihood ratio LR ($\log_{10}\mathrm{LR}^{-1}$ < -20), and (d) and (f) are examples of poorly fitted spectra with high MAD (> 2) and LR ($\log_{10}\mathrm{LR}^{-1}$ > -2) to be rejected by the tests. Thin horizontal lines represent $\log_{10}(\partial T/\partial z)^2 = -4$. All spectra are corrected from the minimum frequency to the cut-off frequency by the frequency response function $\left\{1+\left(2\pi f\tau_0\right)^2\right\}^2$, where the 1/4 attenuation time constant $\tau_0 = 3$ msec. ©American Meteorological Society. Used with permission.

Fig. 3.4. Comparison of 50-m-mean χ (a) and ε (b) from VMP (horizontal axis) and MR (vertical axis). Color of dots denote the fall rate W of MR. Solid and dotted black lines denote $y = x$ and $y = 10^{\pm 1}x$, respectively. ©American Meteorological Society. Used with permission.

Fig. 3.5. Histograms of $\log_{10}(\chi_{MR}/\chi_{VMP})$ (a-c) and $\log_{10}(\varepsilon_{MR}/\varepsilon_{VMP})$ (d-f) for 10 m-mean (a, d), 50 m-mean (b, e), and 200 m-mean (c, f). The "median", "mean", and "SD" of the figures are the median, arithmetic mean, and standard deviation of $\log_{10}\{\chi_{MR}/\chi_{VMP}(\varepsilon_{MR}/\varepsilon_{VMP})\}$. "factor10", and "factor3" are the percentage of data within factors of 10, and 3, respectively. (g, h) Dependence of ratios (in %) of data within factors of 3 (g) and 10 (h) on the averaging depth intervals from 10 m to 200 m. Averaging was performed after PF14 tests (MAD < 2, LR > 100, and SNR > 1.5). The vertical solid, dashed, and dotted black lines in (a)-(f) are $x = 1$, factor 10, and factor 100, respectively. ©American Meteorological Society. Used with permission.

Fig. 3.6. Comparison between CTD-attached MR (red) and free-fall VMP (blue) of the vertical profiles of χ (a), temporal variability of micro-temperature $\partial T'/\partial t$ (b), mean MAD (c), LR^{-1} (d), fall rate W ms^{-1} (e), and standard deviation W_{sd} ms^{-1} (f) of W at Sta.052 observed near the Aleutian Islands (54°59.72N, 172°29.96W). The data in (a) and (c)-(g) were computed from 1-sec bin and then averaged over 10 m after PF14 tests. The data in (b) is raw data sampled at 512 Hz. Temperature gradient spectra at depths with the gray shades in (a) are shown in Fig. 3.7e. ©American Meteorological Society. Used with permission.

Fig. 3.7. Enlarged view of the raw data of micro-temperature (a, b) and fall rate (c, d) at Sta.052, where the fall rate W is computed from raw 64 Hz pressure data. The horizontal thick lines denote $W = 0$. (e) Examples of temperature gradient spectra at the gray shades

of Fig. 3.6a. “p” is the range of pressure over which each spectrum is calculated. ©American Meteorological Society. Used with permission.

Fig. 3.8. Scatter plots of $\log_{10}(\varepsilon_{MR}/\varepsilon_{VMP})$ represented by color shades for MAD and LR^{-1}(a), and for W and W_{sd} (b) for the 50-m averaged MR dataset after PF14 tests. Crosses denote the overestimated data of $\varepsilon_{MR}/\varepsilon_{VMP}$>10, and dots the data with $\log_{10}(\varepsilon_{MR}/\varepsilon_{VMP})$ <10. ©American Meteorological Society. Used with permission.

Fig. 3.9. (a) $\log_{10}(\varepsilon_{MR}/\varepsilon_{VMP})$ represented by color shades for W and W_{sd} based on the 1-m averaged MR data after PF14 tests. (b) Geometric mean distribution of $\varepsilon_{MR}/\varepsilon_{VMP}$ of (a) over the grids of $\Delta x \times \Delta y = 0.1 \times 0.01$ ms^{-1}. (c) Histogram of the $\log_{10}(\varepsilon_{MR}/\varepsilon_{VMP})$ data in (b). The circles in (b) are the data with $0.4 < \log_{10}(\varepsilon_{MR}/\varepsilon_{VMP}) < 0.5$, and the solid line (y = 0.2x – 0.06) is the regression for the circles. ©American Meteorological Society. Used with permission.

Fig. 3.10. The same as Fig. 3.4a-f but for the data after screening overestimated data with the criteria of $W_{sd} > 0.2W$-0.06. Averaging was performed after eliminating data which satisfy $W_{sd} > 0.2W$-0.06, in addition to PF14 tests. The thick curves are the normal distribution for the “mean” and the “SD”. The vertical solid, dashed, and dotted black lines are x=1, factor 10, and factor 100, respectively. ©American Meteorological Society. Used with permission.

Fig. 3.11. Comparison of 50 m-mean χ (a) and ε (b, c) between from VMP and MR after screening the data using the criteria of PF14 tests for bad spectra and $W_{sd} > 0.2W$-0.06 for

overestimated data. In (c), the turbulent energy dissipation rate ε from VMP (horizontal axis) is derived from the shear probes which are the standard sensors for ε. The red and black lines show the 1st order approximation line using principal component analysis in the range of 10^{-11} to 10^{-7}. The red lines are drawn for only $W > 0.9$ ms^{-1}. The solid, broken, and dotted black lines denote $y = x$, $y = 3^{\pm 1}x$ and $y = 10^{\pm 1}x$, respectively. ©American Meteorological Society. Used with permission.

Fig. 3.12. The dependence of the ratios of χ/χ (DP: $\tau_0 = 3$ msec) (a) and ε/ε (DP: $\tau_0 = 3$ msec) (b) on turbulence intensity in the standard double-pole $\tau_0 = 3$ msec case. For the two frequency response functions and time constants τ (Blue: SP10: single-pole $\tau = 10$ msec, cyan: SP04: single-pole $\tau_0 = 4$ msec, red: DP04: double-pole $\tau = 4$ msec, magenta: DP02: double-pole $\tau_0 = 2$ msec). Solid, dashed, and dotted black lines are $y = x$, $y = 2^{\pm 1}x$, and $y = 3^{\pm 1}x$, respectively. ©American Meteorological Society. Used with permission.

Fig. 3.13. Possible influence of insufficient correction and variable fall rate, W, on the spectra (a) and reduction rates (b) of ε and χ for the situation where relatively strong turbulence of $\chi = 10^{-7}$ °C^{2}s^{-1} and $\varepsilon = 10^{-7}$ Wkg^{-1} is measured using a thermistor with the 1/4 time constant $\tau_0 = 3.5$ msec, and is then insufficiently corrected with the faster time constant $\tau_0 = 3$ msec under the variable fall rates from 0.2 to 2 ms^{-1}. ©American Meteorological Society. Used with permission.

Fig. B1. Distributions of the ratios of VMPs deployed at the same location within intervals of 0.2 ~ 2.9 hours. Forty-five VMP observations were performed, and 32 pairs of profiles at the same location within about 2 hours are compared (triangles in Fig. 3.2). χ and ε

were estimated using FP07 thermistors in the same method described in section 2. The legends are the same as those in Fig. 3.10. The thick black curves are normal distributions derived from “mean” and “SD”. The vertical solid, dashed, and dotted black lines are x = 1, factor 10, and factor 100, respectively.

al. 1993). Data are averaged in 320 m segment. The surface data which includes pressure < 100 dBar are not used. In (a), data with pressure > 2000dbar are excluded since accuracy of measurement of LADCP is low in the deep ocean. In (b), data with $N^2 < 10^{-6}$ [s^{-2}] are excluded since estimation of vertical gradient of density is difficult in low stratified regions.

Fig. 4.5. Vertical cross sections of turbulent energy dissipation rate ε_T from CTD-attached thermistor measurements along (a) 137°E (RF16-06) and (b) 47°N (MR-14-04). (a-b) ε_T is averaged over 50 m after removing the data at $W_{sd} > 0.2W$-0.06 and W_{min}. (c) Vertical profile of horizontally averaged ε_T for each section. (d-e) Vertically averaged ε_T below 500 m, in order to exclude the surface dissipation, where the red lines are denoted at $\varepsilon = 10^{-10}$ and 10^{-9} Wkg^{-1}. (f-g) Topographic roughness at each station, defined as the variance of bathymetric height [m^2] obtained from ship depth soundings (version 17.1; Smith and Sandwell, 1997), calculated in 60 km square regions.

Fig. 4.6. (a) Relation between the observed energy dissipation ε_T and stratification represented by squared buoyancy frequency N^2. Colors denote pressure. (b) Histogram of diapycnal diffusivity K_ρ $(= 0.2\varepsilon/N^2)$. The vertical axis denotes data number. 200 m averaged data after data screening is shown.

Fig. 4.7. Relation between depth-integrated observed energy dissipation $\int \rho\, \varepsilon_T \mathrm{d}z$ and model-based depth-integrated baroclinic energy conversion rate Ec (red dots) representing generation of internal waves by tidal forcing, and between $\int \rho\, \varepsilon_T \mathrm{d}z$ and

depth-integrated tide-induced energy dissipation *Ed* (blue dots) for MR-14-04 and RF1606. X-axis: depth-integrated $\rho\varepsilon_T$ at depth from 100 m - bottom excluding surface 100m layer to avoid wind influence. Y-axis: *Ec* and *Ed* are estimated in ON13 from three-dimensional tide-driven model of NH11. *Ec* and *Ed* simulated with the resolution (1/15°) model is multiplied by 1.5 as in ON13. 'r' in legend is correlation coefficient in logarithmic scale and 'mean' is geometric mean of Y/X.

Fig. 4.8. ε_{MODEL} (ON13) along (left panel) 137°E and (right) 47°N. (a)(e) Near-field ε_{NEAR} , (b)(f) far-field ε_{FAR} , (c)(g) background ε_{BACK} , (d)(h) $\varepsilon_{MODEL} = \varepsilon_{NEAR}+\varepsilon_{FAR}+\varepsilon_{BACK}$.

Fig. 4.9. Same as Fig. 4.7 but for modified ε_{MODEL} which is fitted to the observed data.

Fig. 4.10. Comparison of ε (a) from the CTD-attached thermistor observations and (b) from the model (ON13) which reproduced radio-carbon isotope ratio in the Pacific, from (c) a revised model where far-field is proportional to the squared buoyancy frequency N^2 and background value of epsilon is based on the observed minimum diapycnal diffusivity $K_\rho = 10^{-7}$, to make the model distribution close to the observation.

List of Tables

Table 4.2. The geometric means of $\varepsilon_{\mathrm{MODEL}}/\varepsilon_{\mathrm{T}}$ considering the uncertainties in measurements, with confidence interval of bootstrap method. Three values with "-" denote the lowest possible value, the mean and the highest corresponding to the uncertainty of the individual thermistors whose time constant for spectrum double-pole correction range from 1.9 to 5.6 msec based on the result of Chapter 2. Another source of uncertainty is the weak turbulence region of $\varepsilon_{\mathrm{T}} < 10^{-10}$ [Wkg^{-1}] where ε_{T} can be varied between the smallest $\varepsilon_{\mathrm{BACK}} \sim 10^{-11}$-$10^{-12}$ and 10^{-10} as discussed in Chapter 2. The left is for the model of ON13. The right is the revised model where far-field is proportional to the squared buoyancy frequency N^2 and $\varepsilon_{\mathrm{BACK}}$ is based on the observed minimum diapycnal diffusivity $K_{\mathrm{BACK}} = 10^{-7}$ $\mathrm{m^2s^{-1}}$.

Chapter 1

General introduction

1.1 Role of turbulent mixing

Turbulent mixing is one of the main physical processes which control the meridional overturning circulation by vertically transporting heat and materials. Although mean diapycnal diffusivity $O(1)$ cm^2s^{-1} is required to close the global overturning circulation (Munk, 1966; Munk and Wunsch, 1998), observed diffusivity has been an order of magnitude lower in large part of the oceans (e.g. Toole et al., 1994; Ledwell et al., 1993, 1998; Nagasawa et al., 2007). Vertical diffusivity is not uniform in the ocean, but patchy with both depth and location (e.g. Kunze et al., 2006; 2017; Waterhouse et al., 2014; Whalen et al., 2012; 2015), and strong mixing beyond 1 cm^2s^{-1} is observed in specific hotspots with rough topography (e.g. Brazil basin, Polzin et al., 1997; the Izu-Ogasawara Ridge, Nagasawa et al., 2007; the Hawaiian Ridge, Klymak et al., 2006) or near the straits (e.g. Kuril straits, Itoh et al., 2010; 2011; 2014; Yagi and Yasuda, 2012; 2013; Yagi et al., 2014; Tanaka et al. 2014).

Meridional overturning circulations depend on the spatial structure of the vertical diffusivity. For example, structures of the meridional overturning circulation in the North Pacific could be modified by the vertical distribution of diapycnal diffusivity in the Kuril strait as suggested by a numerical model study (Kawasaki and Hasumi, 2010). Tide-induced vertical mixing away from generating regions (far-field mixing) could be also important for the Pacific thermohaline circulation (Oka and Niwa, 2013). Observations of global turbulence distribution with higher resolution in time and space need to be taken to quantify and understand global ocean circulations.

Turbulent vertical mixing is also quite important to quantify and understand diapycnal transports of chemical substances including macro- and micro- nutrients to be supplied to biological production. Vertical turbulent flux of a material is represented by the formula of $\overline{w'C'} = -K_\rho\, \partial \overline{C} / \partial z$ where w' is the vertical velocity of turbulent eddies, C' is the deviation from the mean material concentration $\overline{C}$, and K_ρ is the turbulent diapycnal diffusivity. Enhanced turbulence (mixing hot spot) plays important roles in maintaining high biological productivity through the turbulent diffusive supply of macro- and micro- nutrients such as iron in the northwestern subarctic Pacific (Nishioka et al. 2013; Nishioka and Obata 2017), along the eastern Bering Sea shelf edge (GreenBelt: Tanaka et al. 2012; 2013; 2015) and nitrate in the Kuroshio (Kaneko et al. 2013).

1.2 Indicators of turbulence intensity

One of the indicators of turbulence intensity is the rate of loss of kinetic energy due to molecular viscosity. It is represented as turbulent energy dissipation rate, ε, which is given by the following equation under the assumption of isotropy,

$$\varepsilon = 7.5\nu\langle(\partial u'/\partial z)^2\rangle, \tag{1.1}$$

where ν is the kinematic viscosity, $\partial u'/\partial z$ is the vertical shear of micro-scale (with a few cm spatial scale) horizontal velocity, and the angle brackets $\langle\ \rangle$ is spatial averaging. ε is usually estimated by directly measuring $\partial u'/\partial z$ with an airfoil shear probe.

The energy dissipation rate could also be estimated from micro-temperature by fitting a universal spectrum to an observed temperature gradient spectrum. ε is related to the

Batchelor length scale η_B, where both viscosity and molecular diffusion of temperature becomes effective (Batchelor, 1959), as follows

$$\eta_B = 1/k_B = 2\pi(\nu\kappa^2/\varepsilon)^{1/4}, \tag{1.2}$$

where k_B is the Batchelor wavenumber. In this thesis, the unit of wavenumber is described as cyclic wavenumber, cycle per meter [cpm]. From the above expression (Eq. 1.2), we obtain

$$\varepsilon = (2\pi)^4 k_B^4 \nu\kappa^2, \tag{1.3}$$

This thesis focuses on estimating ε since it is a necessary indicator to evaluate turbulent mixing and diapycnal transport via the diapycnal diffusivity $K_\rho = \Gamma\varepsilon N^{-2}$ (Osborn, 1980), where K_ρ is diapycnal diffusivity, Γ is mixing efficiency, and N is buoyancy frequency. Detail of the way of estimating ε is shown in Chapter 2.2.

1.3 Current turbulence observation

Micro-scale velocity shear and temperature have been measured by using an airfoil shear probe (e.g. Osborn 1974; Osborn and Crawford, 1980) or a fast response thermistor (e.g. Kocsis et al., 1999; Ruddick et al., 2000; Moum et al., 2013), respectively. The former measures micro-scale current variation caused by turbulent eddies, and the latter measures micro-temperature variation with thermistors whose response is much faster than temperature sensors equipped to CTD (Conductivity-Temperature-Depth). Even though it is "fast" response, the very small scale is difficult to be measured, and there are uncertainties in high frequency part of temperature spectra (Gregg, 1999). Accordingly, shear probes have been more widely used in the microstructure measurements than fast-response thermistors. Since micro-velocity measurement is easy to be influenced by noise owing to the vibration of instruments themselves, it has been performed by using special free-fall or free-rise profilers which are designed to stably move in sea water (e.g. Lueck et al., 2002). Since these observations take ship-time and need special skills to be operated, they are difficult to perform widely and frequently. Even in the present day, microstructure observations are limited. Large-scale microstructure observations covering basin-wide top-bottom oceans is thus necessary to evaluate the three-dimensional distribution of turbulence intensity.

1.4 New observational system

In this thesis, we aim to make it to be practical use of a new method to conveniently obtain turbulence data via direct microstructure measurements using an internal-recording profiler attached to a CTD frame. By using this method, we can obtain microstructure data down to the ocean floor at every CTD cast in vast areas than by using a free-fall profiler which needs extra-ship time, special instruments and operational skills. Besides, CTD systems can be equipped with a LADCP (Lowered Acoustic Current Profiler) to concurrently yield fine-scale density and velocity data with microstructure, and the process of energy transport from the tidal wave to turbulence could be discussed.

However, CTD frames are connected with a steel cable and stretched throughout the deployment, and does not fall freely. Therefore, acceleration or deceleration of the cable corresponding to rolling or pitching of a ship as well as winch feeding speed variability causes vibrations which possibly affect microstructure measurements. To establish this CTD-attached microstructure measurement, influence of the frame movement on turbulence estimation and limitations of this measurement method need to be quantified.

Velocity shear probes are much more sensitive to instrument vibrations than thermistors which measure scalar fields. Accordingly, the thermistors are chosen for CTD-attached microstructure sensors in the present thesis.

1.5 Overview of this thesis

Analysis methods of microstructure measurements using CTD-attached fast-response thermistors, are developed in this thesis, to reveal basin-scale turbulence distribution in the northwestern Pacific by using widespread CTD-attached thermistor data from existing CTD observational network. These data could contribute to the state estimate of the general ocean circulation.

One of the problems of this method is the poor temporal response of the fast-response FP07 thermistors, which could affect the estimation of turbulence intensity. Since the availability and limitation of the turbulence measurements with fast-response thermistors have not been quantified, they are assessed in Chapter 2. Another problem is the quaking of the frame due to rolling and pitching of ships. Even though measurements with thermistors are less sensitive to the vibration of instruments than those with shear probes, large quaking is possible to influence on micro-temperature measurement. This influence is quantified in Chapter 3. In Chapter 4, this method is applied to widespread observations. Based on the above assessments, basin scale turbulence distribution in the northwestern Pacific will be revealed from microstructure measurements for the first time.

Chapter 2

Turbulence Estimation Using Fast-Response Thermistors Attached to a Free-Fall Vertical Microstructure Profiler

2.1 Introduction

The FP07 (Fastip Probe, model 07) thermistor, a common type of fast-response thermistors in oceanic observations, is surrounded by glass coating, and this causes a time delay of heat transferring from the surface of the glass coating to the sensor core (Gregg, 1999). The frequency spectrum of temperature is then attenuated in high frequency range (Lueck et al., 1977; Gregg and Meagher, 1980). This possibly influences turbulence estimation, especially in the case of faster sensor speeds where spectra shift to higher frequency.

The form of the attenuation has been proposed to be represented by the single- (Lueck et al., 1977) or double- (Gregg and Meagher, 1980) pole low-pass filter functions by conducting laboratory experiments. Observed temperature gradient spectra could be corrected by multiplying the reciprocal of these low-pass filter functions, though the effectiveness of these correction to estimates of turbulence intensity is scarcely investigated (Kocsisi et al., 1999; Peterson and Fer, 2014; henceforth, PF14).

On the basis of field observational data, Kocsis et al. (1999) evaluated thermistor-derived turbulence intensity by carrying out a comparison of energy dissipation rate ε

from the FP07 thermistors and shear probes with a slowly rising (with the speed of 0.08 ms^{-1}) profiler. After correcting temperature spectra with the single-pole function and the time constant of 7 milli-second (henceforth, msec), they showed both microstructure methods yield nearly the same turbulence intensity. Meanwhile, PF14 used a glider with a moving rate of ~ 0.4 ms^{-1}. The resulting temperature-derived and shear-derived turbulence intensity well agrees by correcting temperature spectra with the single-pole function with the time constant of 12 msec.

Although several studies as above showed the availability of turbulence measurements with FP07 thermistors, there are differences in correction functions and time constants. There seems to be even no consensus on which functions (single-pole or double-pole) and what time constants are appropriate. One of the reasons of the difficulty in determining the sole frequency response function is that it could be different among individual thermistors (Gregg 1999), in observation platforms and in turbulence intensities. To make turbulence measurements with thermistors practical, it is required to make clear correction methods with their quantitative assessment of availability and limitation.

This chapter aims to expand the knowledge of availability of turbulence estimation from fast response thermistors. This chapter reveals 1) effect of correction to the temperature spectrum for the estimate of ε, 2) best correction function for the thermistors to yield ε compatible with ε from the shear probes, and 3) difference in ε between individual thermistors. To achieve above purposes, ε from thermistors is compared with ε from shear probes, which is the common type of sensor in turbulence observation (Lueck et al., 2002). Both of them are attached to the same free-fall microstructure profiler, and performances of thermistor estimation with single- and double-pole frequency response corrections and several time constants in the nominal range are quantified. Section 2.2 provides the procedures for estimating ε. Section 2.3 presents the results of the comparison between thermistors and shear probes. The performances of thermistors in weak turbulence ranges, where measurements with velocity shear probes could be unreliable, are discussed in section 2.4.

2.2 Data and Method

2.2.1 Observational data

Vertical Microstructure Profiler 2000 (henceforth VMP, manufactured by Rockland Scientific International Inc.) was used to measure turbulence fields around the Aleutian Islands, the Kuril straits, and the northwestern Pacific from 2009 to 2016. It was deployed from the stern deck and freely fell at the speed of 0.6 - 0.7 ms^{-1} at a depth of 0 - 2000 m. The VMP was equipped with two velocity shear probes and two FP07 fast response thermistors, produced by Rockland Sci. It was also equipped with Sea Bird temperature (SBE3) and conductivity (SBE4) sensors with a pump (SBE5). A total of 112 VMP profiles were used for comparison between shear probes and thermistors. The details of information about deployments are shown in Table 2.1.

2.2.2 Estimation of ε from velocity shear probes

ε from velocity shear is estimated by integrating a $(\partial u'/\partial z)^2$ spectrum. Accuracy of the shape of the spectrum is confirmed by fitting a universal shear spectrum to the observed one. The form of the universal spectrum in Kolmogorov inertial to viscous range, were advocated theoretically by Corrsin (1964), Saffman (1963), and Panchev and Kesich

(1969). Nasmyth (1970) showed a coherent spectrum by using observed field data. In this paper, a following equation in Oakey (1982) is used.

$$S_{\mathrm{Nasmyth}} = \varepsilon^{3/4} \nu^{-1/4} G2, \qquad (2.1)$$

where $G2 = 8.05(k/2\pi k_{\mathrm{v}})^{1/3}/[1+20(k/2\pi k_{\mathrm{v}})^{3.7}]$ (Wolk et al., 2002), k is a wavenumber, and k_{v} is the Kolmogorov wavenumber ($k_{\mathrm{v}} = (\varepsilon/\nu^3)^{1/4}/2\pi$).

The micro-scale $\partial u'/\partial z$ was high-pass and low-pass filtered to remove shear components with frequency less than 0.25 Hz and more than 98 Hz, and segmented into half-overlapping segments of length about 10 m before Fourier-transformation. Fourier transformations were performed over half-overlapping segments of approximately 1 m, and then spectra were averaged over 10 m. One 10 m-averaged spectrum and ε were thus obtained by using about 20 spectra. These high-pass and low-pass (to avoid aliasing) filters with the mean free-fall speed of 0.6 - 0.8 ms^{-1} could permit VMP to cover the turbulent eddies with the wavenumber of 0.38 - 150 cpm and the length scale of 6.6 mm - 2.6 m, which were able to be resolved assuming that the length scale of the probe and the profiler is 5 mm and 2.5 m, respectively.

An iterative procedure is used to determine ε as follow. First, observed shear spectra are integrated from a minimum wavenumber to an arbitrary wavenumber. Second, ε is estimated via (Eq. 1.1), and then k_{v} is determined. The ε and k_{v} lead to a single form of Nasmyth spectrum via (Eq. 2.1). Third, the ratio between Nasmyth and observed spectra is computed over the range of the wavenumbers from minimum to $0.04k_{\mathrm{v}}$ (near the peak of the Nasmyth spectrum). When the ratio is less (more) than 1/2 (2), interval of integration is spread to 4/3 (reduced to 3/4) of the previous range. This sequence is repeated until the ratio is less than a factor of 2, and then ε is determined. An example of a shear spectrum which is visually regarded as a good agreement with the Nasmyth spectrum is shown in Fig. 2.1a. Shear spectra poorly fitted to the Nasmyth form are not used in the following analysis. ε from the velocity shear, ε_S, is defined as the average of the two shear probes measuring simultaneously. Only data are used such as both of them being regarded as well fitted to the Nasmyth form, and the difference in ε between them are less than 3, since there are natural variabilities in ε with a factor of about 3 (APPENDIX. A).

2.2.3 Estimation of ε from FP07 thermistor observations

Micro-temperature vertical gradient $\partial T'/\partial z$ is also segmented in the same way as velocity shear before Fourier-transformation, although the way of estimating ε and χ, the temperature dissipation rate, are different. They are determined by fitting a universal spectrum to the observed temperature gradient spectrum by using a maximum likelihood estimate (MLE) method, introduced by Ruddick et al. (2000) (henceforth, R00). This method has an advantage for non-Gaussian error distribution, and the MLE estimates are unbiased in comparison with other least squares. Besides, the number of free parameters needed for estimation is reduced by using χ, which is computed by integrating the temperature gradient spectrum after removing instrumental noise. This noise spectrum is here determined from the electrical noise of the instrument in the laboratory bench test (a black curve in Fig. 2.1b). The spectrum is integrated from the minimum wavenumber $k_{\min}$ to the maximum wavenumber $k_{\max}$, where the ratio of the observed to the noise spectra (S/N ratio) is less than 1.5 or the frequency is 165 Hz (cutoff frequency of VMP) if it is less than the frequency of S/N ratio $\approx$ 1.5. Then χ is determined by

$$\chi = 6\kappa \int_{k_{\min}}^{k_{\max}} (S_{\mathrm{obs}} - S_{\mathrm{noise}}) \mathrm{d}k, \tag{2.2}$$

where S_{obs} and S_{noise} are the observed and noise temperature gradient spectrum amplitude at each wavenumber, respectively.

The universal temperature gradient spectrum was firstly introduced by Batchelor (1959) assuming a constant strain rate in the spatial scales smaller than the Kolmogorov length scale, $1/k_{\mathrm{v}}$, and was revised by Kraichnan (1968) including the intermittency of the strain rate. In this thesis, we use Kraichnan universal temperature gradient spectrum $S_{\mathrm{theoretical}}$ with the following form in Roget et al. (2006)

$$S_{\mathrm{theoretical}} = \frac{\chi \cdot q_{\mathrm{K}}^{1/2}}{\kappa \cdot k_{\mathrm{B}}} y_{\mathrm{k}}^{2} \frac{\exp(-\sqrt{6} y_{\mathrm{k}})}{y_{\mathrm{k}}}, \tag{2.3}$$

where $y_{\mathrm{k}} = \sqrt{q_{\mathrm{K}}}k/k_{\mathrm{B}}$ and q_{K} is the Kraichnan constant. q_{K} has been estimated as q_{K} = 3.4 - 7.9 (3.41: Antonia and Orlandi, 2003; 5.26±0.25: Bogucki et al., 1997; 2012, 7.9±2.5: Sanchez et al., 2011). We used a fixed value of q_{K} = 5.26 that was introduced in Bogucki et al. (1997; 2012) and used in PF14.

In the present temperature-based method, ε is determined by fitting the universal spectrum to observed spectra with the MLE, unlike shear-based method by which ε is obtained from just integration of the observed shear spectrum. ε from thermistors thus strongly depends on the accuracy of the fitness to the theoretical spectrum. The best fitted theoretical spectrum is determined via k_{B} by finding the maximum likelihood $C11$ between the observed and theoretical spectra such as

$$C11 = \ln(P) = \sum_{k_{\min}}^{k_{\max}} \ln\left\{\frac{d}{S_{\mathrm{theoretical}}+S_{\mathrm{noise}}} \times \chi_{\mathrm{d}}^{2}\left[\frac{dS_{\mathrm{obs}}}{S_{\mathrm{theoretical}}+S_{\mathrm{noise}}}\right]\right\}, \tag{2.4}$$

where χ_{d}^{2} is the chi-square distribution based on that $S_{\mathrm{obs}}/(S_{\mathrm{theoretical}}+S_{\mathrm{noise}})$ is distributed as a χ_{d}^{2} probability density function with the degrees of freedom d. By applying various k_Bs to S_{obs}, the maximum $C11$ and one k_B are determined, and then ε is obtained via (Eq. 1.3). An example of observed and fitted theoretical temperature gradient spectra with the noise spectrum is shown in Fig. 2.1b.

Poorly fitted spectra were discarded by three quality tests introduced by R00. First, the mean absolute deviation (MAD, defined as Eq. (24) of R00) between the observed and theoretical spectra must be small. The threshold was set at MAD < $2(2/d)^{1/2}$. Second, the signal to noise ratio of spectra (SNR) must be sufficiently large, where signal is defined as S_{obs}-S_{noise}. The threshold in this paper was set at SNR > 1.5 according to PF14, which is more strict and larger than the 1.3 in R00, to ensure reliable data were obtained. Third, the observed spectra must have a sharp roll-off on the higher wavenumber side of the spectrum peak. To ensure this, the likelihood ratio (LR = $P_{(\text{Kraichnan spectrum})}/P_{(\text{straight line})}$) is used. The likelihood $P_{(\text{straight line})}$ from using a straight line fitted to the observed spectrum in log-log space should be smaller than the likelihood $P_{(\text{Kraichnan spectrum})}$ from using universal spectra. If the likelihood ratio is small, the theoretical curve is rejected as it does not provide a significantly better fit than the power law fit. Further details are described in R00. In this thesis, the threshold value of LR is set at LR > 100, similar to R00 and PF14. According to PF14, the LR criterion are unsuitable for power law fitted with a positive slope (for example, Fig. 4d of PF14). Thus, we only apply the LR criterion when the power law fit has a negative slope.

In this chapter, data with potentially double-diffusive condition are not used; only data with turner angle -45° < Tu < 45° (stable) or buoyancy Reynolds number $I = \varepsilon/\left(\nu N^2\right) > 20$ (turbulent) are used, though this does not largely change the results (not shown).

2.2.4 Correction function for temperature gradient spectra

FP07 thermistors are not fast enough to resolve the temperature fluctuation in high wavenumber range, except for slow fall speeds (~ 0.2 ms^{-1}). Temperature spectra are attenuated at high frequency and could sometimes yield underestimated dissipation rates. For practical use, thermistor signal needs to be corrected by applying correction functions to observed temperature gradient spectra. Such correction function is represented by the reciprocal of the frequency response function of the temperature gradient spectrum. The time response of the temperature probe is assumed to be described by the following equation (Fofonoff et al., 1974)

$$T_{\mathrm{true}} = T + \tau \mathrm{d}T/\mathrm{d}t, \tag{2.5}$$

where T is the measured temperature which is smoothed due to the slow thermistor response, T_{true} is the true micro-scale temperature profile, and τ is the time constant which represents response time. By expressing the temperature as a Fourier series, a frequency response function is derived as a single-pole low-pass filter as

$$T/T_{\mathrm{true}} = 1/\left[1+\left(f/f_{\mathrm{c}}\right)^2\right], \tag{2.6}$$

where f is the frequency and f_{c} is the half attenuation frequency at which $T/T_{\mathrm{true}} = 1/2$. Lueck et al. (1977) compared the frequency response of thermistors in a water tunnel with a spectrally calibrated platinum thin film thermometer. They found the theoretical response functions were similar to a single-pole filter in the frequencies lower than 12 Hz.

On the other hand, Gregg and Meagher (1980) found that the response function is formulated by a double-pole low-pass filter (Eq. 2.7) for frequencies less than 25 Hz, although the single-pole was an equally good representation for less than 10 Hz.

$$T/T_{\mathrm{true}} = 1/\left[1+\left(f/f_{\mathrm{c}}\right)^2\right]^2, \tag{2.7}$$

where f_{c} represents the quarter attenuation frequency ($T/T_{\mathrm{true}} = 1/4$). The time constant is defined as the inverse of f_{c}: $\tau = 1/\left(2\pi f_{\mathrm{c}}\right)$ in both single and double-pole functions. The examples of the correction functions are shown in Fig. 2.1. The dependence of the time constant on fall rate*[1] is not included in this thesis.

2.3 Results

2.3.1 In the case without correction

ε_{T} from the seven thermistors*[2] without correction shows a bias which strongly depends on ε_{S} (Fig. 2.2a). Here subscripts T and S denote thermistor and shear probe, respectively. $\varepsilon_{\mathrm{T}} \approx \varepsilon_{\mathrm{S}}$ is only achieved in the range of $\varepsilon_{\mathrm{S}} \sim 10^{-10}$ - 10^{-9} $\mathrm{Wkg^{-1}}$ (henceforth, $\mathrm{Wkg^{-1}}$ of ε unit is omitted). ε_{T} is significantly underestimated for $\varepsilon_{\mathrm{S}} > 10^{-9}$, and most of dots are distributed below the lower dashed line denoting $\varepsilon_{\mathrm{T}}/\varepsilon_{\mathrm{S}} < 1/3$ (see the yellow line in Fig. 2.2b). Since natural variability in turbulence estimation is within a factor of 3 (APPENDIX A), underestimation with the ratio $\varepsilon_{\mathrm{T}}/\varepsilon_{\mathrm{S}} < 1/3$ is defined here to be unacceptable. Underestimation is significant with increasing ε_{S}, and the terrible underestimation ($\varepsilon_{\mathrm{T}}/\varepsilon_{\mathrm{S}} < 1/10$) is seen in the range of $\varepsilon_{\mathrm{S}} > 10^{-7}$. The larger kinetic energy

*[1]: Gregg and Meagher (1980) showed that τ depends on the sensor speed as $\tau = \tau_0 W^{\gamma}$ where $\gamma = -0.32$, while Hill (1987) reported that $\gamma = -0.5$. In this thesis, $\gamma = 0$.

*[2]: In Fig. 2.2 - 2.4, numbers of dots of seven probes are same; 761 dots of each probe compose a total of 5327 dots shown in Fig. 2.2, in order not to emphasis the characteristics of one specific sensor. In Fig. 2.5, number of dots are different between seven probes since they are averaged individually.

dissipation rate is, the larger the Batchelor wavenumber becomes (Eq. 1.3). This means that large k_B are not measured appropriately. This is consistent with the fact that temperature gradient spectra are attenuated in the high frequency range because of the insufficient time response of thermistors.

In the weak turbulence range, $\varepsilon_S < 10^{-10}$, ε_T is also underestimated compared with ε_S by a factor of 3. One reason for this underestimation could come from the measurable limit of the shear probes. The lower limit of shear estimation in the free-fall VMP2000 measurement is $\varepsilon_S \sim (1\text{-}3)\times10^{-10}$ according to manufacturer specifications. Shear probes are generally more sensitive to the vibration of instruments than thermistors which measure scalar field. Thermistors hence could be possible to detect weaker turbulence than shear probes. The case of the weak turbulence will be further discussed in section 2.4.

As mentioned above, the reasons of the underestimation of ε_T are different between in the strong ($\varepsilon_S > 10^{-9}$) and weak ($\varepsilon_S \sim 10^{-10}$) turbulence ranges. We next examine corrections in the strong turbulence range by applying two frequency response functions and several time constants to temperature gradient spectra, and quantify errors between ε_T and ε_S.

2.3.2 In the case with spectrum corrections

The temperature gradient spectra are corrected by multiplying the reciprocal of the frequency response functions shown in the previous studies (Lueck et al., 1977; Gregg and Meagher, 1980). By applying these corrections, ε_T becomes larger in the stronger turbulence range by about 3 - 10 times (Fig. 2.3) where time constants τ_0 are varied in the nominal range; τ_0 = 7±3 msec for the single-pole, which is almost equivalent to τ_0 = 3±1 msec for the double-pole function (henceforth, single-pole and double-pole are SP and DP, respectively).

In the case of the DP (τ_0 = 3 msec) and SP (τ_0 = 7 msec), ε_T and ε_S are compatible in the range of $10^{-10} < \varepsilon_S < 10^{-7}$ Wkg^{-1} because the geometric means of $\varepsilon_T/\varepsilon_S$ are within a factor of 3. Whereas, for $\varepsilon_S > 10^{-7}$, the DP correction is more appropriate than the SP one; the geometric average of $\varepsilon_T/\varepsilon_S$ for 3 msec DP is 0.50, while $\varepsilon_T/\varepsilon_S$ for 7 msec SP is 0.45 (the yellow plot in Fig. 2.4). This is because the DP function amplifies the spectrum more (less) in higher (lower) frequencies significantly than the SP function (Fig. 2.1c). The SP correction may cause the underestimation of ε_T for very large ε_S (> 10^{-7} Wkg^{-1}).

From the above results, it can be concluded that turbulence measurements with the FP07 fast-response thermistors are practically valid by correcting temperature gradient spectrum using the DP (τ_0 = 3 msec) and the SP (τ_0 = 7 msec) functions in the range of $10^{-10} < \varepsilon_S < 10^{-7}$ Wkg^{-1}. This acceptable range covers most of the ocean except for coastal very strong turbulence regions.

2.3.3 Dependence on individual thermistors

It is reported there are differences in glass coatings among individual thermistors even for the same type of FP07s (Gregg, 1999). Frequency response and estimate of ε_T depend on this difference in individual thermistors. However, time constant and its diversity have not been quantified. In this subsection, ε_T of seven FP07 thermistors are compared with simultaneously measured ε_S in order to make clear τ_0 and its uncertainty range, which are important to estimate uncertainty in thermistor-based turbulence measurements.

It should be noted that ε_T is consistent with ε_S and within a factor of 3 for all the thermistors examined here. Whereas dependence of ε_T estimate on individual thermistors are evident as shown in Fig. 2.5, some thermistors (S/N 886,1024 and 1025) show that ε_T larger than ε_S in the whole range of $10^{-10} < \varepsilon_S < 10^{-7}$ Wkg^{-1}, while other thermistors (S/N 271 and 285) show smaller values, even after all the temperature gradient spectra were corrected by the same SP and DP correction functions with τ_0 = 7 and 3 msec respectively. This scatter is possibly caused by the one of time constant τ_0 due to the differences in glass coatings. Degree of the scatter depends on turbulence intensity ε_S; the difference between probes is a factor of 3 in the relatively strong turbulence of $\varepsilon_S \sim 10^{-7.5}$ Wkg^{-1}, while it is within a factor of 2 in the relatively weak turbulence of $\varepsilon_S \sim 10^{-9.5}$ Wkg^{-1}. This dependence of scatter on the turbulence intensity ε_S is due to the shift of spectra to higher frequency range where attenuation is more considerable.

We are able to estimate the time constant τ_0 for individual thermistors by adjusting ε_T to ε_S. The optimal τ_0 range between 3.0 and 10.2 msec for the SP, and 1.9 and 5.6 msec for the DP functions. This result means the τ_0 uncertainty of thermistors with unknown time constant is in the above ranges. The range is roughly consistent with the nominal value of the time constant 7±3 msec for the single-pole function.

From the results, errors derived from the uncertainty of time constants should be considered to be at least 3.0 - 10.2 (SP) or 1.9 - 5.6 (DP), which cause the uncertainty of ε_T estimate with a factor of about 3. For the accurate estimation with a factor less than 3, each probe should be calibrated by comparing ε_T with ε_S in field observations as in the present study or in laboratory experiments (e.g. Lueck et al., 1977; Gregg and Meagher, 1980).

2.4 Discussion

2.4.1 Measurement limit in the strong turbulence and its dependence on sensor moving speed

The present study shows ε_{T} is best matched to ε_{S} in the case where the double-pole correction function with the time constant of 3 msec is applied to observed temperature gradient spectra. However, $\log_{10}(\varepsilon_{\mathrm{T}}/\varepsilon_{\mathrm{S}})$ in Fig. 2.3 shows slight decreasing trend with ε_{S} for increasing $\varepsilon_{\mathrm{S}} > 10^{-8}$ Wkg^{-1}. This slight decreasing trend of $\varepsilon_{\mathrm{T}}/\varepsilon_{\mathrm{S}}$ could be due to the insufficient correction in high frequency ranges.

In stronger turbulence fields, spectra shift to higher wavenumber (and thus higher frequency) where spectra might not be fully corrected. This could cause the underestimation of χ and ε. Since the Batchelor wavenumber is represented as $k_{\mathrm{B}} = k_{\mathrm{P}}\sqrt{6q_{\mathrm{K}}}$ via d(Eq. 2.3)$/dk = 0$, where k_{P} is the wavenumber at the spectral peak, ε_{T} is represented by

$$\varepsilon_{\mathrm{T}} = (2\pi)^4 \left(6q_{\mathrm{K}}\right)^2 f_{\mathrm{P}}^4 / W^4 \nu \kappa^2, \tag{2.8}$$

where $f_{\mathrm{P}} = k_{\mathrm{P}} W$ is the spectral peak frequency, assuming the falling speed W is constant. ε_{T} is thus a function of $\left(f_{\mathrm{P}}/W\right)^4$.

The horizontal axis of Fig. 2.3 can be converted from ε_{S} to the peak frequency f_{P} via (Eq. 2.8) as shown in Fig. 2.6, where $\log_{10}(\varepsilon_{\mathrm{T}}/\varepsilon_{\mathrm{S}})$ severely depends on the peak frequency f_{P} in the case without correction. Even though the half attenuation frequency of 23 Hz (equivalent with the time constant of 7 msec in the single-pole correction) is expected, $\varepsilon_T/\varepsilon_S$ is less than 1/3 for f_P > 10 Hz as shown in the black curves in Fig. 2.6. Without any corrections, the maximum acceptable ε_T is 3×10^{-9} Wkg^{-1} at which the black curve crosses $\varepsilon_T/\varepsilon_S$ = 1/3 in Fig. 2.6. This maximum acceptable ε_T changes with variable falling speed because the peak wavenumber $f_P = k_P W$ that yields ε_T via (Eq. 2.8); the maximum limit could be 7×10^{-6} ($\approx 3\times10^{-9}\times(0.1/0.7)^{-4}$) Wkg^{-1} for W = 0.1 ms^{-1}, and could be 7×10^{-10} ($\approx 3\times10^{-9}\times(1.0/0.7)^{-4}$) Wkg^{-1} for W = 1.0 ms^{-1}. These indicate that the maximum limit heavily depends on the falling (moving) speed; for the slow-moving platforms correction is not necessary even for the strong turbulence field, whereas for the faster speed correction is inevitable even for the weak turbulence field. In the case without correction, the maximum limit can be estimated as above.

In the case with correction, the estimate of the maximum limit is not straightforward, because the peak frequency f_P also changes by multiplying the correction functions (Eq. 2.6 for the single-pole and Eq. 2.7 for the double-pole). The peak frequency f_P shifts to be higher by amplifying spectra at greater frequency. For the double-pole correction with τ_0 = 3 msec and the falling speed of W = 0.6 - 0.8 ms^{-1}, the maximum peak frequency $f_P \approx$ 30 Hz beyond which there is no data in the present study as shown in the magenta curve in Fig. 2.6b. This could yield the maximum limit of ε_T for variable falling or moving speed W via (Eq. 2.8). For W = 0.7 and f_P = 30, the maximum limit of ε_T will be 5×10^{-7} Wkg^{-1}. Since ε_T is proportional to $\left(f_P/W\right)^4$, the maximum limit of ε_T would shrinks to 1×10^{-7} ($\approx 5\times(1/0.7)^{-4}\times10^{-7}$ Wkg^{-1}) for W = 1 ms^{-1}.

The variable correction functions and time constants in the previous studies (Kocsis et al., 1999; PF14) could be explained by the diversity of sensor moving (falling) speed

W and turbulence intensity of target water. Qualitatively, for larger moving (falling) speed W, the maximum limit of ε_T decreases with a function of W^{-4} for the same correction function and time constant. To measure strongly turbulent water, double-pole function and/or larger time constants are necessary to recover the attenuated spectra. Previous studies using the single-pole correction (Kocsis et al., 1999; PF14) were conducted with relatively smaller moving speed (0.08 ms^{-1} in Kocsis et al., 1999; 0.4 ms^{-1} in PF14) than in the present study (0.6 - 0.8 ms^{-1}).

2.4.2 Thermistor microstructure measurements under anisotropy

In large part of the ocean interior, especially from intermediate to deep Pacific over smooth bottom topography, turbulent energy dissipation rate is weak and ε < 10^{-10} Wkg^{-1} (e.g. Gregg and Sanford, 1988). In such a weak turbulence, estimations from shear probes are not reliable owing to the influence from instrumental noise. The present study shows that turbulent energy dissipation rates from thermistor, ε_T are generally much (one or two order of magnitude) less than ε_S for ε_S < 10^{-10} Wkg^{-1}. This small ε_T could represent real turbulence situations because the thermistor is less sensitive to the vibration and motions of profilers and noise level could be lower than that of shear probes.

However, we need to be careful about the thermistor measurements because the performance of thermistor measurements under weak turbulence has not been well examined. In particular, isotropic assumption, under which Batchelor or Kraichnan theories are established, might not be fully satisfied in such weak turbulence fields. In this subsection, we discuss the availability of thermistor measurements in weak and anisotropic turbulence.

For shear probe measurements under anisotropic turbulence, Yamazaki and Osborn (1990) showed that ε_S from vertical shear of turbulent velocity under the assumption of isotropy is greater by at most 35 % than the true ε even for the anisotropic condition of $20 < I < 100$, where the buoyancy Reynolds number, $I = \varepsilon/\left(\nu N^2\right)$, is an indicator of isotropy. $I < 100$ is regarded as anisotropy (Gargett, et al., 1984; Gargett, 1985).

In the anisotropic range ($20 < I < 100$) where observed ε_S is reliable ($\varepsilon_S > 3\times10^{-10}$ Wkg^{-1}), $\log_{10}(\varepsilon_T/\varepsilon_S)$ is within the reasonable range ($1/3 < \varepsilon_T/\varepsilon_S < 3$) as shown in Fig. 2.7, where the thick red line denoting 21-point running mean of $\log_{10}(\varepsilon_T/\varepsilon_S)$ is within a factor of 3 denoted by the black dashed lines. This indicates that ε_T estimate is compatible to the shear probe estimate even in the anisotropic range of $20 < I < 100$. In the case without correction (the thin red line in Fig. 2.7), $\varepsilon_T/\varepsilon_S$ is a little less, but $\varepsilon_T/\varepsilon_S$ is still at around the reasonable range and whether the correction is applied or not does not largely change ε_T. This is because the weak turbulence estimation mainly uses the low frequency components that are not strongly influenced by attenuation.

In the range of $I < 20$, anisotropy is further developed, and the shear probe data with $\varepsilon_S < 10^{-10}$ Wkg^{-1} are less than the lower limit of the manufacturer's specification and could be unreliable. That is, turbulence estimates from velocity shear and temperature are largely different. We need further discussion in this weak turbulence range of $I < 20$ or $\varepsilon_S < 10^{-10}$ Wkg^{-1}.

According to the direct numerical simulations (DNS) by Shih et al. (2005), diapycnal diffusivity plus molecular diffusivity $K_\rho+\kappa$ is $0.2\varepsilon/N^2$ which is the same as in Osborn (1980), and thus $\left(K_\rho+\kappa\right)/\kappa = 0.2PrI$ for $7 < I < 100$, where the Prandtl number Pr is defined as ν/κ. Whereas for $I < 7$, K_ρ becomes equivalent to κ (~ 10^{-7} m^{2}s^{-1}). From another DNS under anisotropy for small I (Godeferd and Staquet, 2003), turbulent thermal dissipation rate χ and K_T are reduced to 5/9 of the ones under isotropic approximation.

Relationship between I and K_T is here examined with the present data to see which (shear or temperature)-based ε is consistent with the above DNS results, as shown in Fig. 2.8, where $I = \varepsilon/\left(\nu N^2\right)$ with the temperature-based ε_T (red dots in Fig. 2.8) and with the shear-based ε_S (blue dots in Fig. 2.8) and $K_T = 5/9 \times \chi/[2(\partial \overline{T}/\partial z)^2]$ for data which satisfy $\varepsilon_T < 10^{-10}$ Wkg^{-1}, and -45° < Tu < 45° at which the Turner angle Tu is in the range without double diffusion.

The relationships between I and K_T (Fig. 2.8) show that the temperature-based estimate is more consistent with the above DNS results. K_T/κ (red dots in Fig. 2.8) takes less than 10 for the temperature-based $I < 1$ indicating, and increases with the slope similar to the one from the DNS for $7 < I < 20$. On the other hand, for the shear-based I (blue dots in Fig. 2.8), K_T is much less than the one from the DNS for $7 < I < 20$ where the DNS suggests that K_T would take much larger values and increase with I.

Let us return to the observed spectra with the large difference between ε_T and ε_S in the weak turbulence ($\varepsilon_T < 10^{-12}$ and $\varepsilon_S < 10^{-10}$), because appropriate measurements have been judged by the form of observed spectra. Both the observed shear (Fig. 2.9a) and temperature gradient (Fig. 2.9b) spectra (black curves) does not significantly deviate from the Nasmyth and Kraichnan universal spectra (cyan and magenta) respectively.

On the other hand, it is noted that the levels of the observed shear spectra are nearly the same order of magnitude (1 - 10 times) with the lowest shear spectrum in all the data (blue curves in Fig. 2.9a), while all the observed temperature gradient spectra are larger than the lowest temperature gradient spectrum by more than 10 times (red and magenta curves). The shear spectrum corresponding to this lowest temperature gradient spectrum denoted by the blue curve in Fig. 2.9a indicates that the observed shear spectra are not discernable from noise if we assume that the lowest spectra are in the noise level. Spectrum shape is hence not the appropriate way to judge the reliability of measurements in such weak turbulence. The present study implies that noise should be also considered for the measurement in the weak turbulence regime.

These suggest that the shear spectra are influenced by instrumental noise although they look fitted to the Nasmyth spectra and that the temperature-based estimate is more reliable in the weak turbulence regime at least from the observed spectrum analysis in the present study. Since anisotropy also could influence the universal spectra derived under the assumption of isotropy, further analysis and theoretical studies are required to reveal which the temperature- or shear-derived method is the reliable in the weak turbulence regime.

APPENDIX A

Natural variability in ε_S

There is an acceptable error coming from natural variability in estimating turbulence intensity. Energy dissipation rates from velocity shear ε_S are somewhat different between two shear probes S1 and S2 (Fig. A1), even though they simultaneously measured micro-velocity shear at a distance less than 5 cm. Here S1 and S2 denote the first and second shear probes of VMP. Dots in Fig. A1 are not located closely along the solid straight line which indicates $\varepsilon_{S1} = \varepsilon_{S2}$, but scattered around this line. According to

Oakey (1982) who compared two simultaneously measured shear probes, ε has natural variability with a factor of 2. Thus, the ratio of ε_{S1} and ε_{S2} from two independent probes could be scattered within a factor of $2.8 = \sqrt{2^2+2^2}$ based on the law of error propagation. Actually, most plots (89 %) of Fig. A1 are distributed within the dashed lines which denotes $\varepsilon_{S1} = 3^{\pm1}\varepsilon_{S2}$. The acceptable errors derived from natural variability in the simultaneous measurements is defined as the factor of 3. Shear-based ε_S data are used for comparison with temperature-based ε_T, only when the ratios of S1 and S2 are between 1/3 and 3.

Table and Figure Captions

Table 2.1. List of serial numbers of FP07 probes, cruise and ship, period (year/month) and area of VMP2000 observations. T1 and T2 are the first and second probes. Number of dots is different between Fig. 2.2-2.4 and 2.5.

S/N of FP07	Cruise name	ship name	term	area	number of dots (τ_0=0) Fig. 2.2-2.4, 2.5
271 (T1)	KH-09-4	Hakuho-maru	2009/Aug-Sep	Aleutian	761, 1292
285 (T2)	KH-09-4	Hakuho-maru	2009/ Aug-Sep	Aleutian	761, 1281
415 (T1)	Go11	Gordienko	2011/ Jul-Aug	Kuril	761, 4626
883 (T1)	Mu14	Multanovskiy	2014/Jun-Jul	Kuril	761, 761
886 (T2)	Mu14	Multanovskiy	2014/Jun-Jul	Kuril	761, 765
1024 (T1)	KH-16-3	Hakuho-maru	2016/Jun	NW Pacific	761, 3649
1025 (T2)	KH-16-3	Hakuho-maru	2016/6	NW Pacific	761, 3622

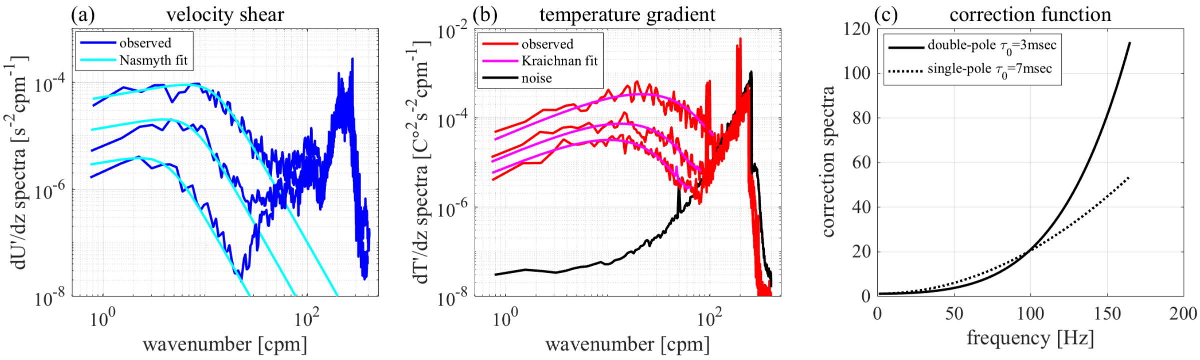

Fig. 2.1. Examples of spectra of (a) velocity shear and (b) vertical temperature gradient. The blue and red curves denote the observed spectra and the cyan and magenta curves represent the fitted Nasmyth (Eq. 2.1) and Kraichnan spectra (Eq. 2.3), respectively. In (b), the black curve denotes a noise spectrum used to determine the range for fitting. (c) Correction functions to temperature gradient spectra. The solid curve is the double-pole function $[1+(2\pi f\tau_0)^2]^2$ with $\tau_0 = 3$ msec and the dotted curve is the single-pole function $[1+(2\pi f\tau_0)^2]$ with $\tau_0 = 7$ msec. The temperature gradient spectra in (b) are corrected by the double-pole function with $\tau_0 = 3$ msec.

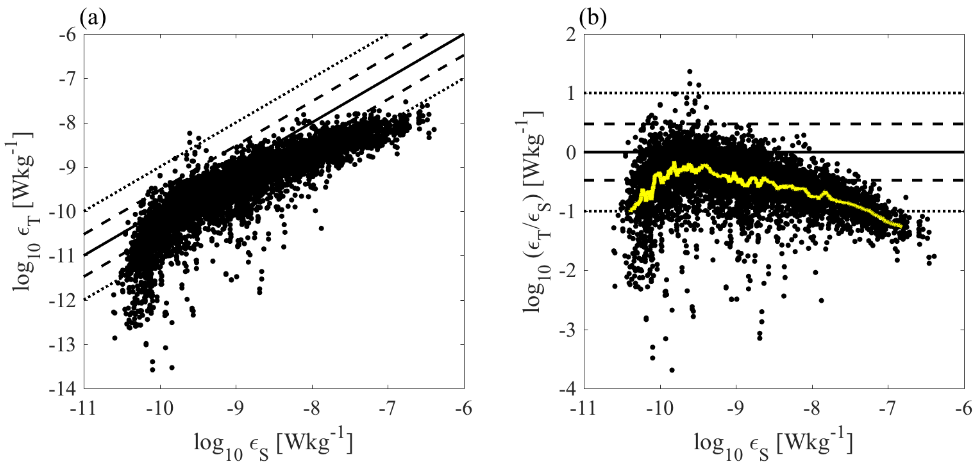

Fig. 2.2. Comparison of concurrently measured turbulence dissipation rates ε_T from thermistors and ε_S from shear probes in the case without correction of temperature spectra. (a) Scatter plot of ε_T versus ε_S in logarithmic coordinates. (b) Dependence of the ratio $\log_{10}(\varepsilon_T/\varepsilon_S)$ on ε_S. The solid line represents $\varepsilon_T = \varepsilon_S$, the dashed lines $\varepsilon_T = 3^{\pm 1}\varepsilon_S$, and dotted lines $\varepsilon_T = 10^{\pm 1}\varepsilon_S$. The yellow curve in (b) denotes the 101-point running mean of $\log_{10}(\varepsilon_T/\varepsilon_S)$.

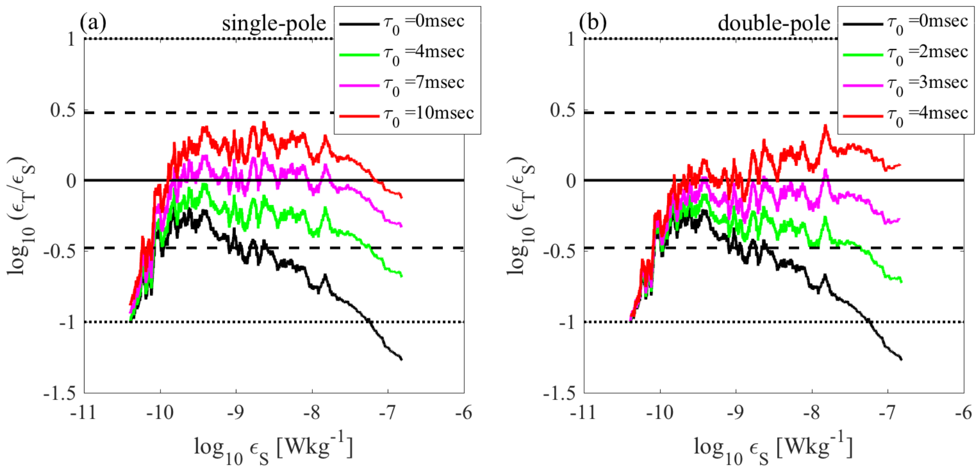

Fig. 2.3. Same as Fig. 2.2b but for the dependence of the time constant τ_0 (shown by color) in the case of (a) the single-pole correction (Eq. 2.6) and (b) the double-pole correction (Eq. 2.7). The black, green, magenta, red curves represent 101-point running-mean of $\log_{10}(\varepsilon_T/\varepsilon_S)$ for τ_0 = 0 (same as the yellow curve in Fig. 2.2b), 4, 7, and 10 msec in (a), and for τ_0 = 0, 2, 3, and 4 msec in (b).

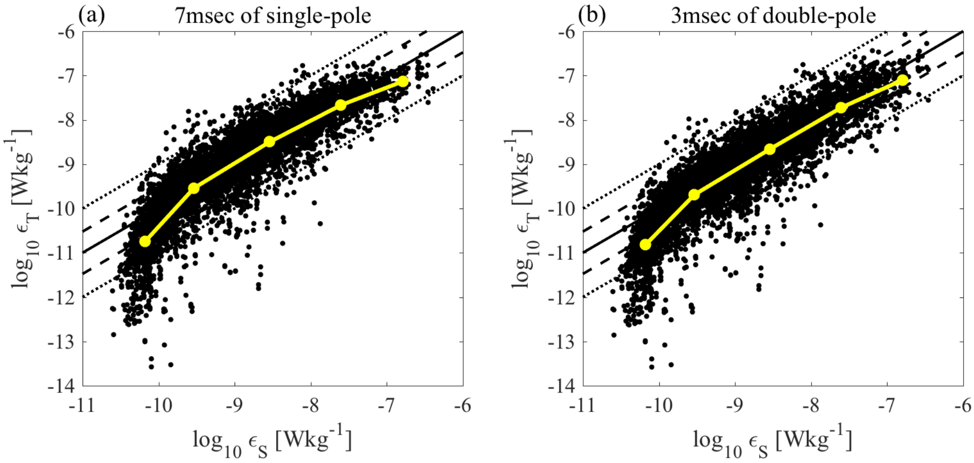

Fig. 2.4. Same as Fig. 2.2a but for the data after applying (a) the single-pole and (b) the double-pole corrections to spectra with the time constant of τ_0 = 7 msec and τ_0 = 3 msec, respectively. The yellow dots with lines are the geometric mean of ε_T and ε_S in the ranges of $10^{-(i+1)} < \varepsilon_S < 10^{-i}$ for i = 6, 7, …10.

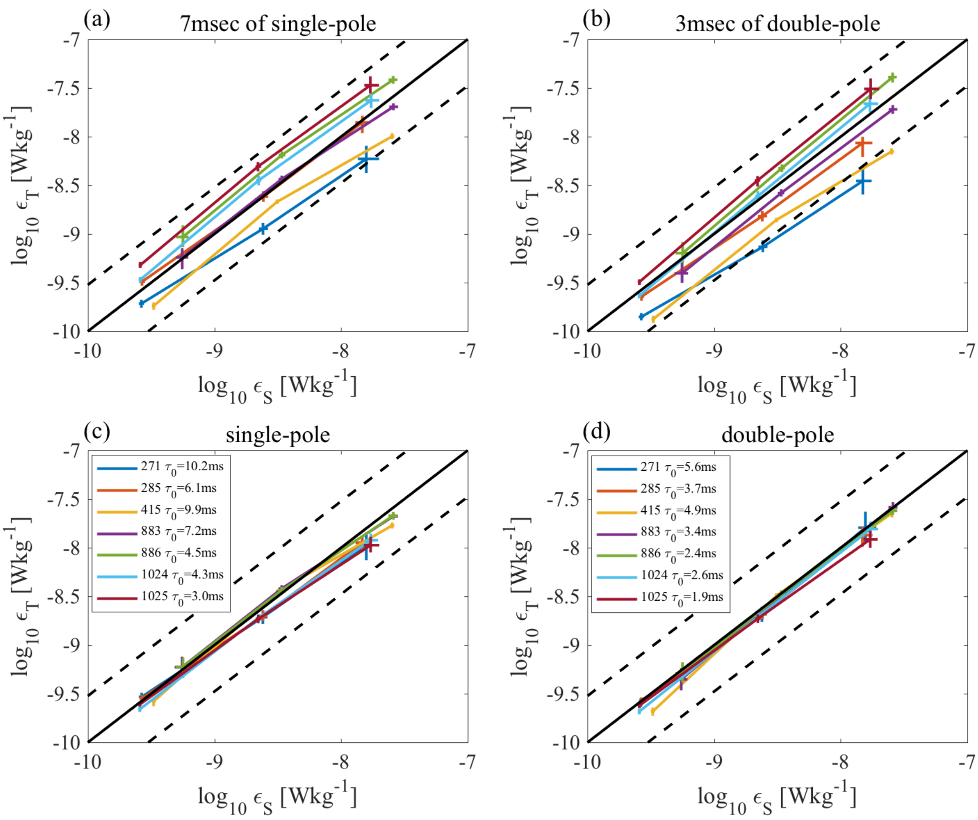

Fig. 2.5. Dependence of the ε_T-ε_S relation on the time constant τ_0 of individual FP07 thermistors. The plus marks with lines are the geometric means of ε_T in the ranges of $10^{-(i+1)} < \varepsilon_S < 10^{-i}$ (i = 7, 8, 9). (a) single-pole correction with τ_0 = 7 msec and (b) double-pole correction with τ_0 = 3 msec. (c, d) For the cases where optimally computed τ_0 by minimizing $\log_{10}|\varepsilon_T/\varepsilon_S|$ are used for (c) single- and (d) double-pole corrections.

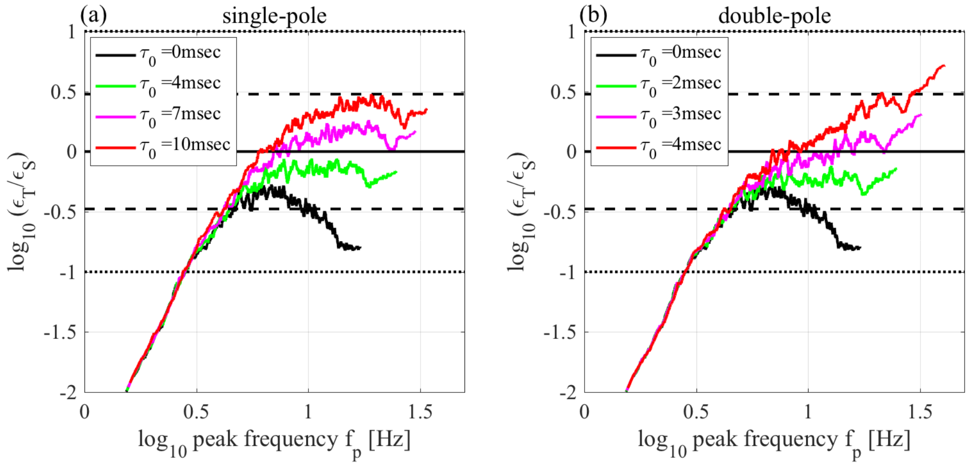

Fig. 2.6. Dependence of the ratio $\log_{10}(\varepsilon_T/\varepsilon_S)$ on the frequency at the peak of the Kraichnan fitted spectra, f_p, which is corrected by (a) the single-pole and (b) the double-pole frequency response functions with the time constant of τ_0 = (a) 4, 7, 10 and (b) 2, 3, 4 msec. Colored curves represent 101-point running means as in Fig. 2.3.

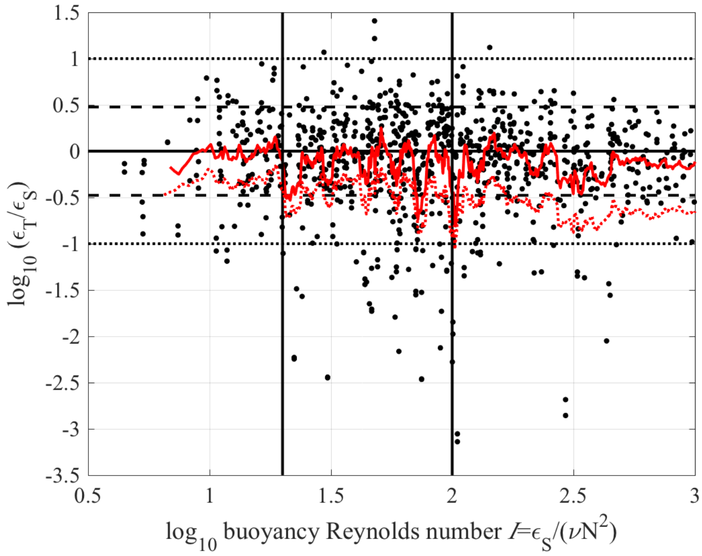

Fig. 2.7. Dependence of $\log_{10}(\varepsilon_T/\varepsilon_S)$ on the buoyancy Reynolds number $I = \varepsilon_S/\left(\nu N^2\right)$. Dots denote the data satisfying $\varepsilon_S > 3\times10^{-10}$ $\mathrm{Wkg^{-1}}$ from seven probes. Temperature spectra are corrected by the double-pole functions with the time constant of 3 msec. The thick red curve represents the 21-points running mean of the dots. The thin red curve represents the 21-point running mean data in the case of without correction. Vertical solid lines indicate I = 20 and 100 between which ε_S are reliably estimated in spite of the violation of isotropic turbulence assumption.

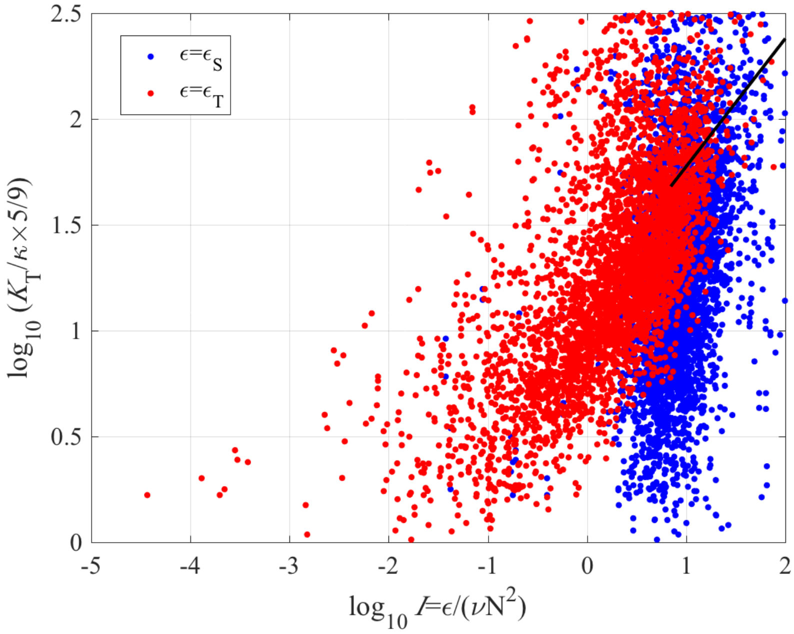

Fig. 2.8. Dependence of $\log_{10}(K_T/\kappa)$ (the ratio of the total thermal diffusivity divided by the molecular thermal diffusivity) on the buoyancy Reynolds number *I*. Data of $\varepsilon_T < 10^{-10}$ (weak turbulence) and -45° < *Tu* < 45° (in this Turner angle *Tu* range, no double diffusion occurs) is shown from the seven probes. Blue (red) dots represent data using ε_S (ε_T) to calculate *I*. The solid line is $y = 0.2Prx$ over $7 < I < 100$, where Prandl number $Pr = \nu/\kappa$ is set at the constant value of 12.

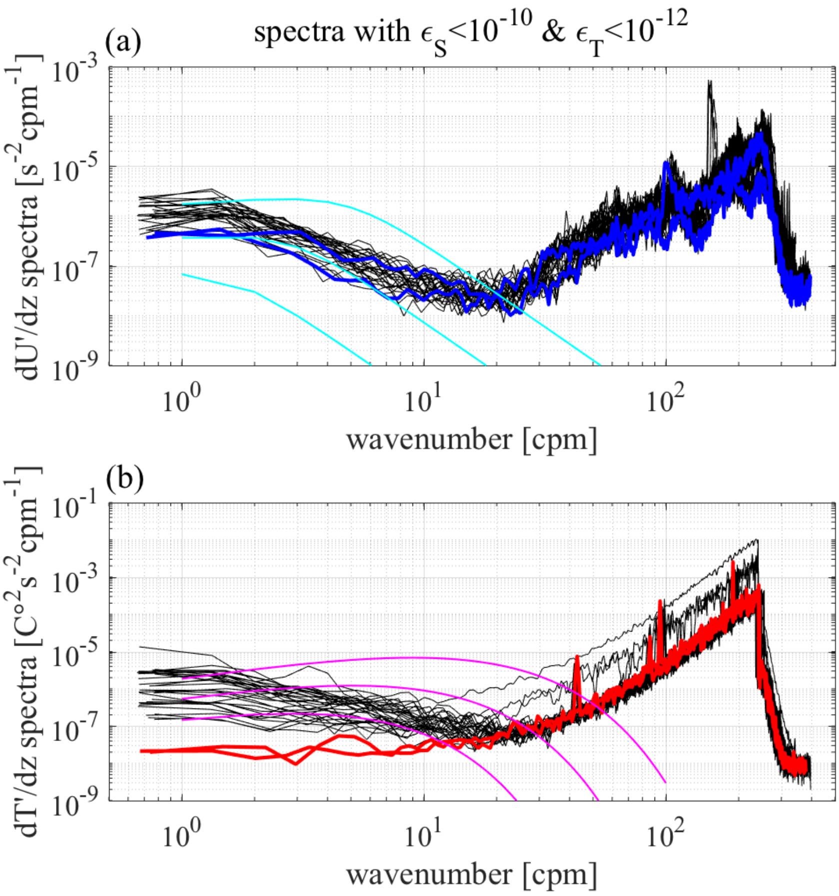

Fig. 2.9. Examples of (a) velocity shear spectra and (b) temperature gradient spectra in the weak turbulence range of $\varepsilon_S < 10^{-10}$ and $\varepsilon_T < 10^{-12}$ Wkg^{-1} from the data in Fig. 2.2. Black curves are observed spectra. All the temperature spectra passed the criterion tests of PF14. Cyan and magenta are the universal Nasmyth and Kraichnan spectra, respectively for $\varepsilon, \chi = 10^{-12}, 10^{-11}, 10^{-10}$. Blue and red curves denote the spectra with the minimum (a) ε_S and (b) χ for S1, S2, T1, and T2 sensors.

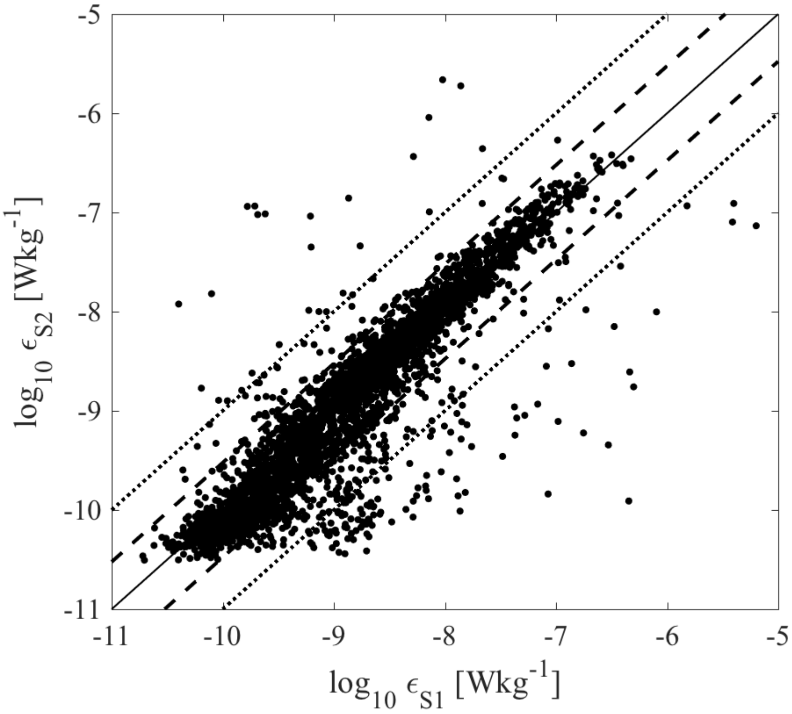

Fig. A1. Scatter plots showing the difference between ε_{S1} and ε_{S2}, where they are from concurrently measured two shear probes S1 and S2. Data with poorly fitted spectra to the Nasmyth spectrum is not used.

Chapter 3

Comparison of turbulence intensity from CTD-attached and free-fall microstructure profilers

3.1 Introduction

In this chapter, a new method is evaluated for obtaining turbulence data via direct microstructure measurements using an internally-recording profiler attached to a CTD frame. Using this method, we can obtain much more microstructure data to the ocean floor from every CTD cast in a vast area than we would use free-fall profilers, which would require extra ship-time, special instruments and operational skills.

A problem of this method is the motion of the CTD frame. It is connected to a steel cable and stretched throughout the deployment, and does not fall freely. Therefore, acceleration or deceleration of the frame due to the rolling or pitching of a ship, as well as variability of the winch feeding speed, causes instrument vibration that could affect microstructure measurements. Although micro-temperature measurements conducted using a fast response FP07 thermistor are less sensitive to vibration than velocity measurements with an airfoil shear probe, there is no consensus on the appropriate usage of an FP07 thermistor attached to the CTD frame. To achieve CTD-attached microstructure measurements, the influence of the frame movement on turbulence estimation and the limitations of this measurement technique are quantified in this chapter.

To our knowledge, only Holmes et al. (2016) have described the use of a micro-temperature sensor attached to a CTD frame, but they did not provide validation of the method. They used data only from times when the CTD package was descending faster than 0.4 ms^{-1}, probably to exclude bad data caused by the "not-free-fall" CTD-attached observation. Earlier, Moum and Nash (2009) used thermistors attached to moorings and demonstrated that the estimated turbulence intensity is comparable to that from a free-fall profiler (Perlin and Moum, 2012), suggesting that CTD-attached thermistors would allow us to measure turbulence fields more frequently and efficiently. Here, we evaluate CTD-attached measurements through comparison with data measured with a standard free-fall profiler, and we identify objective editing criteria for removing abnormal data caused by "not-free-fall" measurements.

The objective of this chapter is to establish a method of using the CTD-attached microstructure profiler for practical use. For this, we compare estimates of turbulence intensity from CTD-attached thermistors to estimates from nearly simultaneous free-fall microstructure profiles. The results of the comparison, including derivation of editing criteria are presented in section 3.3. Uncertainties of estimation derived from CTD-attached thermistors are then discussed in section 3.4.

3.2 Data and analysis

3.2.1 Observational data

A Micro Rider 6000 (henceforth MR), manufactured by Rockland Sci. Int., is an internally recording microstructure profiler to be attached to an observational platform, such as a CTD frame. FP07 micro-temperature sensors were set near the bottom of the frame (Fig. 3.1). 72 profiles of CTD-attached MR observations were performed in the three cruises (Fig. 3.2); 12 profiles were conducted near the Aleutian Passage from August to September 2009 using the R/V Hakuho-Maru (henceforth KH-09-4), 20 profiles around the Tokara Strait in June 2015 using the R/V Shinsei-Maru (KS-15-5), and 40 profiles in the Pacific Ocean in June 2016 using the R/V Hakuho-Maru (KH-16-3). In KH-16-3, a AFP07 microstructure profiler, manufactured by Rockland Sci. Int., was used (Fig. 3.1b). Henceforth, AFP07 is also referred to as “MR” for simplicity. For every MR observation, a microstructure observation was performed using a free-fall Vertical Microstructure Profiler 2000 (henceforth VMP) just before or after the CTD-attached MR observations, within a period of 2 hours. Turbulence intensity from the FP07 thermistors was examined by comparing the MR data with the VMP data.

The most notable difference between the CTD-attached MR and the free-fall VMP is the fall rates. The fall rate W [ms^{-1}] of the MR were usually larger (~ 1.0 ms^{-1}) than those of VMP (0.6 - 0.8 ms^{-1}). The fall rates of MR were slow near the surface and the bottom. The other difference is the cutoff frequency; 165 Hz for VMP and 98 Hz for MR and AFP07.

3.2.2 Analysis method of turbulence intensity

Most of the analyses for estimating ε are the same as in Chapter 2, and thus omitted here. One difference in estimation between Chapters 2 and 3 is the length of spatial bin for estimating one spectrum and ε. In this chapter, the length is set at 1 second (henceforth, 1 sec), while it was set at about 10 m (corresponds to 14 sec for $W = 0.7$) in the Chapter 2. This is because wavenumber spectrum has to be calculated using the samples during which the fall rate W is constant, based on the Taylor frozen hypothesis (Thorpe, 2007). In the case of the CTD-attached method, W is dependent on winch feeding speed and ship motion because the frame is pulled by a wire throughout casts. Given the actual variation of W with time owing to the heave of the wire (see Fig. 3.7c, d), spectrum should be calculated using a smaller segment than 10 m, where W is regarded as nearly constant. Accordingly, it is set at 1 sec, as small as to resolve 10 cm to 1 m scale. The interval for VMP is also set at 1 sec in order to compare them at the same depth.

The other difference is upward motion of the instrument. When the CTD frame is moving down at a slower speed, there would be a moment when the frame rises, unlike VMP. This creates artificial turbulence at the bottom of the frame where the microstructure sensors are located. The 1-sec-binned data with decreased pressure readings were not used, even when the decrease was instantaneous. Furthermore, only data of the new water is measured; i.e., data with pressure during which the CTD rises and measurements after having the direction reversed are not used to exclude wake contamination.

For qualification of temperature spectra, PF14 criterion tests are applied also in this chapter after correcting spectra by the double-pole low-pass filter function with the time constant of 3 msec. Examples of temperature gradient spectra passed and rejected by these tests are presented in Fig. 3.3.

3.3 Results

3.3.1 Comparison between MR and VMP

Firstly, χ and ε at the same locations and depths were compared between VMP and MR (Fig. 3.4), where χ and ε were arithmetically averaged over 50 m depth segments. Data (especially with the red dots in Fig. 3.4 representing higher (> 0.9 ms^{-1}) fall rates) are distributed roughly along the $y = x$ line, whereas excessively large χ and ε from MR (blue dots representing lower (< 0.5 ms^{-1}) fall rates in Fig. 3.4a) are identified. Turbulence intensity from MR that is more than 10 times larger than that from VMP is referred to as "MR/VMP>10" or "overestimated data". For χ and ε, 12.3 % and 15.9 % of data are distributed above the $y = 10x$ lines, while 5.8 % and 6.0 % are distributed below the $y = 1/10x$ lines, respectively. The overestimation of MR data is thus greater than the underestimation in both ε than χ.

The pairs of MR and VMP observations used for comparison in Fig. 3.4 were not performed at the same time, but separately within about 2 hours. Considering the intermittent characteristics of turbulence and its spatial variability, the data from MR and VMP do not need to be identical; even two shear probes separated by several centimeters yield scattered results with a factor of 3 (Chapter 2 and Goto et al., 2016, henceforth, GYN16). Similarity with some scatter is expected for the pairs of MR and VMP observations taken within about 2 hours, considering that micro-scale (order of 1 cm - 1 m) turbulence is related to the larger vertical (order of 10 - 100 m) and time scales (order of hours - day) of internal wave fields (e.g. Henyey et al. 1986). Here, we use $\log_{10}(\chi_{MR}/\chi_{VMP})$ and $\log_{10}(\varepsilon_{MR}/\varepsilon_{VMP})$ distributions (Fig. 3.5) to check the similarity and scatter between MR and VMP by comparing them with consecutive free-fall VMP observations performed within about 2 hours (APPENDIX).

A large portion of the MR data is consistent with VMP data, based on the $\log_{10}(\chi_{MR}/\chi_{VMP})$ and $\log_{10}(\varepsilon_{MR}/\varepsilon_{VMP})$ distributions (Fig. 3.5). 10 m-mean χ_{MR}/χ_{VMP} and $\varepsilon_{MR}/\varepsilon_{VMP}$ (Figs. 3.5a and 3.5d) show log-normal distributions, with medians of around 1 ($\log_{10}(\chi_{MR}/\chi_{VMP}) = -0.02$ and $\log_{10}(\varepsilon_{MR}/\varepsilon_{VMP}) = -0.04$) and scatters, indicating that MR ≈ VMP. Scatter is represented by the standard deviation, *SD*, and the mean±1.96×*SD* covers 95 % of data. For the 10 m-mean χ and ε, SD = 1.07 and 1.30 respectively; the data is thus approximately within a factor of 100. This scatter is similar to that of the repeated free-fall VMP observations at the same locations within about 2 hours, as shown in the appendix where the natural temporal variability of turbulence is examined and the width of the distribution is represented by 1.96×*SD* = 1.96×1.01 (Fig. B1a).

With larger averaging bin-length, scatters of the distributions decrease and data within factors of 3 and 10 increase for both the comparisons of χ and ε between MR and VMP (Figs. 3.5g, h) and among the repeated VMP observations (Fig. B1 and Table B1). Data within a factor of 3 increased from 39 % for the 10m-mean χ to 61 % for the 200m-mean (Figs. 3.5a-c).

From the histograms for the 50 m and 200 m -mean comparisons (Figs. 3.5bc and 3.5ef), the data that deviated from the log-normal distributions become noticeable in the range of MR/VMP > 10 which corresponds to the overestimated MR measurements (Fig. 3.4). These data that deviated from symmetric log-normal distributions are regarded as unusual, considering that the distributions of repeated VMP observations are symmetrical and 95 % of the data are within a factor of about 10 (*SD* = 0.36 ~ 0.70) (Figs. B1bc and B1ef). Data satisfying MR/VMP > 10 in the 50 m-mean are then defined as overestimated data.

3.3.2 Overestimation and disturbed spectra related to fall rate variability

The MR overestimates could be related to the "not-free fall" measurements. The CTD frame to which the MR was attached connected to a winch on deck through a steel wire, and ship rolling and pitching changed the lowering rate of the CTD (henceforth, referred to as the fall rate), thus the moving CTD frame may generate disturbance. The fall rate is the most noticeable difference between the MR and VMP observations. In this subsection, the influence of fall rate variability on the overestimates and temperature gradient spectra are described with an example of vertical profiles (Fig. 3.6).

Fall rate variability may generate disturbance of the temperature microstructure. χ estimated from MR (red curves in Fig. 3.6a) is much larger than χ from VMP (blue) at 0-100, 400-600, and 1000-1100 dbar. At these depths, fall rate W (Fig. 3.6e) is small, and the standard deviation of W, W_{sd} [ms^{-1}], (Fig. 3.6f) is large. Here W is computed from the finite difference of the pressure, which is sampled at 64 Hz and interpolated into 512 Hz. W_{sd} is the standard deviation of the fall rate over 1 sec. This correspondence between χ and (W_{sd}, W) suggests that MR measurements are bad due to the fall rate variability. Micro-temperature temporal variability $\partial T/\partial t$ is large at these depths, indicating that raw micro-temperature is influenced even before performing spectral analysis.

The enlarged view of $\partial T/\partial t$ and the raw fall rate before averaging (Fig. 3.7) shows the impact of fall rate variability on micro-temperature. Even when the fall rates were positive and the thermistors entered into new water, large micro-temperature variations occurred in the period during which the fall rates took minima. This correspondence suggests wake generation from the CTD frame when the frame slows and then accelerates, even though spectra have passed quality tests with the PF14 criteria (Fig. 3.7e).

The dependence of overestimated ε of MR on the spectrum shape (MAD, LR) and on the fall rate variability (W, W_{sd}) was quantified by compiling all the 50 m-depth averaged data (Fig. 3.8). The overestimated data with $\varepsilon_{\mathrm{MR}}/\varepsilon_{\mathrm{VMP}} > 10$ increases with increasing LR^{-1}[*3], especially for $\log_{10}(\mathrm{LR}^{-1}) > -10$ (Fig. 3.8a), where about 40 % of the data are

[*3]: 10 m (50 m)-mean $\log_{10}(\mathrm{LR}^{-1})$ in Fig. 3.6d (3.8) was computed by averaging 1-sec LR^{-1} for 10 m (50 m) intervals and then taking logarithm. This is because LR varies

overestimated. This indicated that the spectrum shape tended to be disturbed for the overestimated data. MAD, however, is not sensitive to the overestimation, and overestimated data are distributed uniformly in the MAD range of 0.6 - 1.0.

Overestimates are better separated by W and W_{sd} (Fig. 3.8b) than by the spectrum shape presented by LR^{-1} and MAD (Fig. 3.8a). Overestimated data appear for relatively small W and large W_{sd} (Fig. 3.8b), similarly as seen in Figs 3.6 and 3.7. Fall rate and its variability are thus good indicators for detecting and eliminating overestimated MR data. These results are from the 50-m-depth averaged data, which include about 50 1-sec spectrum data computed from 512 micro-temperature and 64 pressure raw data. If the 50-m data were found to be overestimated and rejected, a large gap in the 50-m data would appear. To reduce such gaps as much as possible, it is better to judge and exclude data averaging as short as possible.

For the 1 m-mean data (which is similar to the 1-s original spectrum data for $W \sim 1$ ms^{-1}), overestimated data ($\varepsilon_{MR}/\varepsilon_{VMP} > 10$) are also found for small W and large W_{sd} (Fig. 3.9a), as found for the 50 m-mean data (Fig. 3.8b), with some scatters, as indicated by the color of dots. To clearly identify the parameter range where the overestimates prevailed, the data in Fig. 3.9a were further averaged in the parameter space (W, W_{sd}) with 0.1 by 0.01 ms^{-1} intervals to indicate correspondence between $\varepsilon_{MR}/\varepsilon_{VMP}$ and fall rate parameters (W, W_{sd}) (Fig. 3.9b). This Fig. 3.9b suggests a simple criterion that separates the overestimated data from the form of $W_{sd} > aW + b$, where a and b are determined as follows. The histogram of $\log_{10}(\varepsilon_{MR}/\varepsilon_{VMP})$ (Fig. 3.9c), based on the data in Fig. 3.9b, shows that $\log_{10}(\varepsilon_{MR}/\varepsilon_{VMP})$ largely deviated from a log-normal distribution for

---

exponentially and the features of small LR are masked when the LR themselves are averaged arithmetically.

$\log_{10}(\varepsilon_{MR}/\varepsilon_{VMP}) > 0.5$. A 1st order regression through points with $0.4 < \log_{10}(\varepsilon_{MR}/\varepsilon_{VMP}) < 0.5$, which separates a border of overestimation, is $W_{sd} = 0.2W - 0.06$ (circles and solid line of Fig. 3.9b).

3.3.3 MR data after screening overestimated data

By removing 1-s data with $W_{sd} = 0.2W - 0.06$, the consistency between VMP and MR is improved, based on the better log-normal distributions (Fig. 3.10). Comparing Fig. 3.10 with Fig. 3.5 shows that most of the overestimation in Fig. 3.5 is removed. The percentage of overestimated data from MR/VMP > 10 was reduced from 12.3 % to 5.8 % and 15.9 % to 4.1 % for the 50 m-bin χ and ε, respectively. Data within a factor of 10 increased from 82 % to 93 % and 75 % to 94 % for the 200 m-depth mean χ and ε, respectively. The ratio of data within a factor of 10 for the 50 m-depth mean also increased. The scatters, represented by *SD*, for the 50 m and 200 m-depth mean ε data are now comparable with the scatters of the repeated VMP observations with the natural temporal variability of turbulence, as shown in the APPENDIX B.

Improvement of the consistency between MR and VMP is noticeable in the scatter plots based on the 50 m-depth averaged data after screening (Fig. 3.11) compared to those before screening (Fig. 3.4). Most of the data from MR are within a factor of 10, and the regression lines based on the principal component analysis are along $y = x$ (black thick lines in Fig. 3.11), especially for the comparison between ε_{MR} and ε_{VMP} which were measured with velocity shear probes attached to the free-fall VMP (Fig. 3.11c).

In contrast, slight underestimation of ε from MR become noticeable after removing overestimated data. It is noted that the median and mean of $\log_{10}(\varepsilon_{MR}/\varepsilon_{VMP})$ in Fig. 3.10 decrease compared with those in Fig. 3.5, and the median and mean of $\log_{10}(\varepsilon_{MR}/\varepsilon_{VMP})$

decrease from -0.09 and 0.57 (Fig. 3.5f) to -0.21 and -0.18 (Fig. 3.10f), respectively, for the 200 m depth-averaged ε.

This ε_{MR} underestimation is also seen in scatter plots (Figs. 3.11b and 3.11c), indicating that MR tends to be underestimated in a strong turbulence environment for higher fall rates ($W > 0.9$ ms^{-1}). The W of a large part of the underestimated data seen in $y < x$ for $\varepsilon_{VMP} > 10^{-9}$ Wkg^{-1} in Fig. 3.11b and 11c are greater than 0.9 ms^{-1} (represented by the red dots in Fig. 3.11), also indicated by the slope of the regression line for data with $W > 0.9$ ms^{-1} (red lines in Fig. 3.11b), which is less than 1. In the range of $y > x$ for $\varepsilon_{VMP} > 10^{-9}$ Wkg^{-1}, in contrast, the green-blue dots representing $W < 0.7$ ms^{-1} prevail (Figs. 3.11b and 3.11c). This dependence on W are also seen in the thermal dissipation rate χ (blue dots in $y > x$ and red dots in $y < x$ for $\chi_{VMP} > 10^{-9}$ in Fig. 3.11a), although the overall underestimation of χ is not noticeable from the regression lines in Fig. 3.11a.

Comparison of χ and ε between the free-fall VMP and not-free-fall CTD-attached MR measurements after screening overestimated abnormal data is summarized in Table 3.1. Acceptable measurements here (the means±their 95 % confidence interval) are within a factor of 3 from the VMP data. The turbulence intensity ranges of acceptable measurements depend on depth-averaging length. χ is acceptable from 10^{-10} to 10^{-7} °C^{2}s^{-1}, in that the average of $\log_{10}(\chi_{MR}/\chi_{VMP})$ is within a factor of 3 ($\log_{10}3 = 0.4771$) for the 10 - 200 m-averaged data. For the 10m and 20m-mean, χ is acceptable but slightly underestimated ($\log_{10}(\chi_{MR}/\chi_{VMP}) = -0.411$ and -0.242 respectively) as seen in Fig. 3.11a. ε is acceptable from 10^{-10} to 10^{-8} Wkg^{-1} for the 20 - 200 m-averaged data, and from 10^{-10} to 10^{-9} Wkg^{-1} for the 10-m data. ε from MR is underestimated for strong turbulence of $\varepsilon > 10^{-8}$ (10^{-9}) Wkg^{-1} for the 20 - 200 m (10 m) averaged data.

3.4 Discussion

3.4.1 Underestimates of energy dissipation rate ε from MR in strong turbulence fields

As shown in section 3c, ε from the CTD-attached MR measurements tends to be underestimated for faster fall rates and in a relatively strong turbulence environment. Here, we discuss the possible reasons of underestimation. As stated in the introduction, turbulence intensity measured with fast-response thermistors tends to be underestimated in strong turbulence environments if the correction to amplify the high-frequency part of the signal is not applied. This is because the response of the thermistors, with half attenuation times of ~ 7 msec for a single-pole function (Lueck et al., 1977), is not sufficient to resolve the high-frequency (and thus high-wavenumber) part of the temperature gradient spectra in strong turbulence regions. By amplifying the high-frequency part of the spectra with the double-pole correction function (Gregg and Meagher, 1980) with a 1/4 attenuation time constant of 3 msec, ε from the thermistors is reported to be acceptable, within a range of 10^{-10} to 10^{-7} $\mathrm{Wkg^{-1}}$, by comparing simultaneously measured ε from shear probes attached to free-fall VMPs, with a fall rate of 0.6 - 0.7 $\mathrm{ms^{-1}}$ (Chapter 2 and GYN16).

The underestimation of MR is partly explained by the higher fall rate, W, of MR (~ 1 $\mathrm{ms^{-1}}$) than the W of free-fall VMPs (~ 0.7 $\mathrm{ms^{-1}}$). ε from thermistors is determined practically by detecting the frequency at the spectrum peak, f_p, through $\varepsilon=(2\pi)^4(6q_K)^2 f_p^4 W^{-4} \nu\kappa^2$. This is derived via Eq. (2.7) and $dS_{\mathrm{theoretical}}/k = 0$. As peak frequency f_p increases with W and $\varepsilon^{1/4}$, the frequency spectrum with larger W and ε shifts to a higher frequency where insufficient thermistor response attenuates the spectra;

the degree of underestimation hence increases with increasing fall rate W and turbulence intensity. According to the above formulae, the acceptable upper limit of 10^{-7} $\mathrm{Wkg^{-1}}$ of ε in the case of $W \sim 0.7$ $\mathrm{ms^{-1}}$ for the free-fall VMP (Chapter 2) would be reduced to 2.4×10^{-8} $\mathrm{Wkg^{-1}}$ ($\sim 10^{-7}\times(1/0.7)^{-4}$) in the case of $W \sim 1$ $\mathrm{ms^{-1}}$ for the CTD-attached MR.

Another possible explanation for the underestimation of MR is that the temporal response of the MR thermistors is slower than that of VMP. Turbulence intensity is variable within a factor of 3 by changing frequency response functions and time constants within the uncertainty of manufacturer specification; single-pole half attenuation time constant τ_0 = 4 - 10 msec, or corresponding double-pole 1/4 attenuation time constant τ_0 = 2 - 4 msec (Fig. 3.12). The acceptable upper limit of ε would be reduced to $\sim0.6\times10^{-8}$ $\mathrm{Wkg^{-1}}$ ($\sim 2.4\times10^{-8}/(3^2 + 3^2)^{1/2}$), which is consistent with that for the 20 - 200 m depth average in this study (Table 3.1).

It is also noted that ε (Fig. 3.12b) is more sensitive to variable correction functions and time constants than χ (Fig. 3.12a). ε is estimated by detecting the wavenumber k_p at temperature gradient spectrum peak, which would be sensitive to spectrum attenuation. χ, however, is estimated by integrating spectra (Chapter 2.2). The difference in procedures for estimating turbulence intensity with spectrum attenuation could cause the sensitivity difference.

The combined impacts of insufficient correction and variable fall rate, W, on the reduction rates of ε and χ are evaluated (Fig. 3.13b) in the case where a relatively strong turbulence with $\chi = 10^{-7}$ $\mathrm{°C^2s^{-1}}$ and $\varepsilon = 10^{-7}$ $\mathrm{Wkg^{-1}}$ is measured using a thermistor, with a 1/4 time constant τ_0 = 3.5 msec, and is then insufficiently corrected using the faster time constant τ_0 = 3 msec under variable fall rates from 0.2 to 2 $\mathrm{ms^{-1}}$ (Fig. 3.13). This situation was reproduced by the following procedures: the temperature gradient Kraichnan spectrum (outermost curve in Fig. 3.13a) with χ = 10^{-7} °C^2s^{-1} and ε = 10^{-7} Wkg^{-1} is first attenuated by the double-pole low-pass filter with the time constant τ_0 = 3.5 msec, and then amplified by double-pole correction with τ = 3 msec under variable fall rates from 0.2 to 2 ms^{-1} (Fig. 3.13a). The wavenumber of the spectrum peak decreases as the fall rate increases, and estimated ε and χ become smaller than their true values (Fig. 3.13b). Reduction of ε is more significant than that of χ. The difference in reduction between ε and χ influences the estimation of the mixing coefficient defined as $\Gamma = \chi N^2/(2\varepsilon\overline{\theta_z}^2)$ (e.g. Gregg et al., 2017). Insufficient thermistor corrections and a large W could lead to a larger mixing coefficient than the true values, as shown in Fig. 3.13b.

Although nominal uncertainty of the time constant yields uncertainty of turbulence intensity within a maximum factor of 3, it is required for reducing uncertainty under large fall rate situations. To reduce the uncertainty of the estimated CTD-attached turbulence measurements, it is necessary to know accurate correction function and time constant for individual thermistor, especially for a fall rate of ~1 ms^{-1}.

3.4.2 Potential reasons for overestimation

The correspondence between the overestimates of MR and a large W_{sd} and small W indicates that the fall rate variability of CTD influences turbulence estimation. The CTD frame descends at varying fall rates which depend on winch feeding speed and ship motions. Descending CTD-frame and attached instruments (CTD, Lowered-Acoustic-Doppler-Current-Profiler or bottles) drag adjacent water and generate turbulent wake, usually above the frame and instruments (on the downstream side). On the other hand, when the CTD-package decelerates more rapidly than the wake which has downward momentum, the wake may be sampled at lowered W by the micro-temperature sensor as the large $|\partial T/\partial t|$ in Fig. 3.7. These could be reasons why the overestimation observed in this study corresponds to large W_{sd} and small W. Such artificial turbulent wake would depend on the space where the thermistors are located: a greater impact is expected for a narrow and crowded space. Thus, the threshold of $W_{sd} = 0.2W - 0.06$ may not be always a typical threshold.

3.4.3 Availability and issues

Fig. 3.7 suggested that W alone could be a good indicator for detecting artificial turbulence due to the wake generated from the CTD-frame. When W is used as a sole criterion, overestimated data can be reduced (the bottom 3 rows of Table 3.2). It is close to the notation of Holmes et al. (2016), who only used data with fall rates larger than 0.4 ms^{-1}, although they did not discuss the validity of CTD-attached measurements and thresholds. For the present dataset, a threshold of $W = 0.4$ ms^{-1} (Holmes et al. 2016) reduces overestimation to 6.1 % by removing 11,643 1-s-binned data, whereas the criterion used ($W_{sd} > 0.2$ W -0.06) reduces it to 4.1 % by removing 14,134 data points. The ratio of data between the factor of 10 is 91 % (hence 9 % is beyond the factor of 10) from the consecutively performed VMP in Fig. B1e, thus the half 4.5 % on the overestimated side is the required ratio for rejecting overestimated data. The ratio (4.1 %) with the criteria in this study is consistent, whereas the criteria with the ratio greater than 4.5 % in Table 2 including the criteria of $W < 0.4$ ms^{-1} could be insufficient for rejecting overestimated data. For more strict criteria, overestimated data reduces, but removed data increases. The choices of criteria hence depend on scientific purposes and measurement environments, such as locations and space of thermistors, and the fall speed regulation system of CTD-winches.

Another difference between the present study and Holms et al. (2016) is the estimate of ε in the present study, whereas Holms et al. (2016) estimated χ where thermistor responses were reported to be calibrated with thermo-couples with faster responses. The present study confirmed the availability of the CTD-attached thermistor method by comparing ε from thermistors with free-fall VMP performed within 2 hours, whereas Holms et al. (2016) did not discuss the validity of the CTD-attached method. Further comparison between Holmes et al. (2016) and the present study could contribute to turbulence estimation from fast-response thermistors attached to a CTD frame.

The CTD-attached method may not be appropriate at depths near the surface or bottom because fall rates are usually set to be slow and sensors easily suffer wake contamination. In contrast, an advantage of the CTD-attached method is easier microstructure measurement in the deep ocean, where $\varepsilon < 10^{-8}$ Wkg^{-1} (upper limit using the present CTD-attached method) in areas of the ocean with depths greater than 500 m (Kunze et al., 2006). The performance of this CTD-attached method depends on oceanic states (calm or rough sea) and the type of winch. To improve performance, using high-tech heave-motion winches which feed cables at constant rates, in addition to setting probes away from other instruments such as CTD and LADCP, would be suitable.

Another issue is the thermistor response (functional form and time constant) of individual FP07 thermistors. Calibration of thermistors by simultaneous measurement with shear probes, thermistors with known responses (GYN16) and thermos-couples (Nash et al., 1999; Moum and Nash, 2009) in wide ranges of turbulence intensity and fall rates could contribute to further improvement of turbulence measurements with the CTD-attached thermistors.

In terms of performance of the fast response thermistor during the faster fall rate, further quantification should be done by comparing them with shear probes, because the upper limit of measurable turbulence from the thermistor must depend on the fall rate as well as the frequency response of individual probe.

APPENDIX B

Temporal variability of $\varepsilon_{\mathrm{VMP}}$

Histograms (distributions) of the ratios of turbulence intensity obtained from repeated VMP casts within 2 hours are presented to show distributions with natural variability of turbulence fields (Fig. B1), where the medians and log-mean are less than 0.05, approximately 95 % of data are within a factor of 100 for the 10-m data (1.96×*SD* ~ 2), and 95 % data are within a factor of 10 for the 50 and 200-m data (1.96×*SD* ~ 1). By comparing these distributions (Fig. B1) with those in Fig. 3.5, the overestimated data in Fig. 3.5 are unusual beyond natural variability.

Variability (scatter represented by the ratio of data within a factor of 3 or 10) of χ and ε distributions differs at each site (Table B1). Large percentages in the table indicate small variability. Variability (scatters) in Sagami Bay is lower than those of Aleutians and Kerama Gap. This could be because bottom topography in the low variability sites is less rough than in sites with large variability. The time intervals of observations in Sagami Bay are less than those in Aleutians and the Kerama Gap. This could be another reason for the difference of variability.

Table and Figure Captions

Table 3.1. Logarithmic mean ("log mean") and its upper and lower boundaries of 95 %, confidence interval with bootstrap method ("95 % bootstrap±") of (left) $\log_{10}(\chi_{MR}/\chi_{VMP})$ and (right) $\log_{10}(\varepsilon_{MR}/\varepsilon_{VMP})$ for the 10 m - 200 m depth-averaged data. Boldface: data within a factor of 3 ($|\log_{10}(\varepsilon_{MR}/\varepsilon_{VMP})| < 0.477$).

		$\log_{10}(\chi_{MR}/\chi_{VMP})$			$\log_{10}(\varepsilon_{MR}/\varepsilon_{VMP})$		
		-10 ~ -9	-9 ~ -8	-8 ~ -7	-10 ~ -9	-9 ~ -8	-8 ~ -7
10m	95% bootstrap+	**0.046**	**-0.117**	**-0.357**	**-0.120**	-0.529	-1.004
	log mean	**0.007**	**-0.159**	**-0.411**	**-0.149**	-0.566	-1.077
	95% bootstrap-	**-0.031**	**-0.203**	**-0.467**	**-0.173**	-0.607	-1.148
20m	95% bootstrap+	**0.081**	**-0.055**	**-0.180**	**-0.053**	**-0.413**	-0.861
	log mean	**0.025**	**-0.104**	**-0.242**	**-0.083**	**-0.459**	-0.937
	95% bootstrap-	**-0.012**	**-0.149**	**-0.311**	**-0.110**	-0.504	-1.017
50m	95% bootstrap+	**0.047**	**-0.031**	**0.044**	**-0.035**	**-0.269**	-0.673
	log mean	**-0.022**	**-0.097**	**-0.038**	**-0.072**	**-0.327**	-0.778
	95% bootstrap-	**-0.075**	**-0.155**	**-0.124**	**-0.111**	**-0.376**	-0.866
100m	95% bootstrap+	**0.007**	**-0.007**	**0.122**	**-0.055**	**-0.207**	-0.592
	log mean	**-0.072**	**-0.085**	**0.006**	**-0.102**	**-0.275**	-0.704
	95% bootstrap-	**-0.149**	**-0.151**	**-0.082**	**-0.143**	**-0.342**	-0.819
200m	95% bootstrap+	**-0.018**	**0.050**	**0.126**	**-0.040**	**-0.159**	-0.519
	log mean	**-0.101**	**-0.048**	**-0.009**	**-0.097**	**-0.243**	-0.659
	95% bootstrap-	**-0.180**	**-0.140**	**-0.121**	**-0.152**	**-0.331**	-0.778

Table 3.2. Number of removed 1-s bin and ratio (in %) of overestimated data after the 50 m mean for various rejection criteria. Boldface: the case presented in Figs. 3.10~3.12.

rejection criterion	number of removed data	% of $\varepsilon_{MR}/\varepsilon_{VMP}>10$
$W_{sd}>0.1W-0.02$	15308	4.6
$W_{sd}>0.1W-0.04$	25393	3.1
$W_{sd}>0.2W-0.04$	9588	5.9
$W_{sd}>0.2W-0.06$	**14134**	**4.1**
$W_{sd}>0.3W-0.08$	10149	4.8
$W_{sd}>0.3W-0.10$	13445	4.2
$W_{sd}>0.4W-0.12$	10467	4.8
$W_{sd}>0.4W-0.14$	13025	4.2
$W<0.40$	11643	6.1
$W<0.45$	14659	5.0
$W<0.46$	15277	4.8

Table B1. Ratios (in %) of χ_{VMP} (3rd-7th row) and ε_{VMP} (8-10th row) between the pair of consecutive free-fall VMPs within a factor of 3, 10, and 100, for the 10m-, 50m- and 200m-depth averaged data. These data are demonstrated for evaluating natural temporal variability of turbulence within two hours as compared between ε_{MR} and ε_{VMP}. Locations of the 45 VMP stations are shown as the triangles in Fig. 3.1.

		Aleutians	Open ocean	Sagami Bay	Kerama Gap	All
number of observations		14	5	10	16	45
number of compared pairs		7	3	9	13	32
time difference (hour)		0.2~2.9	0.3~1.1	0.2~0.7	0.7~2.8	0.2~2.9
χ	10m (factor 3, 10, 100 [%])	32.2 59.1 89.4	45.4 77.9 97.5	51.0 80.0 98.4	36.6 68.0 95.5	38.5 69.3 95.4
	50m (factor 3, 10, 100 [%])	51.1 74.5 100	58.3 94.4 100	59.0 90.2 98	53.6 84.2 99.4	54.4 84.8 99.4
	200m (factor 3, 10, 100 [%])	40.0 73.3 100	70.0 100 100	83.3 100 100	71.4 97.8 100	69.4 95.5 100
ε	10m (factor 3, 10, 100 [%])	42.3 69.7 97.1	37.4 79.1 99.4	39.6 72.2 93.1	40.7 71.3 96	40.4 71.9 96.0
	50m (factor 3, 10, 100 [%])	59.6 91.5 100	55.6 97.2 100	65.6 93.4 97	59.5 89.6 100	60.0 90.8 99.4
	200m (factor 3, 10, 100 [%])	73.3 100 100	70.0 90 100	77.8 100 100	81.3 100 100	79.1 99.3 100

(a) (b)

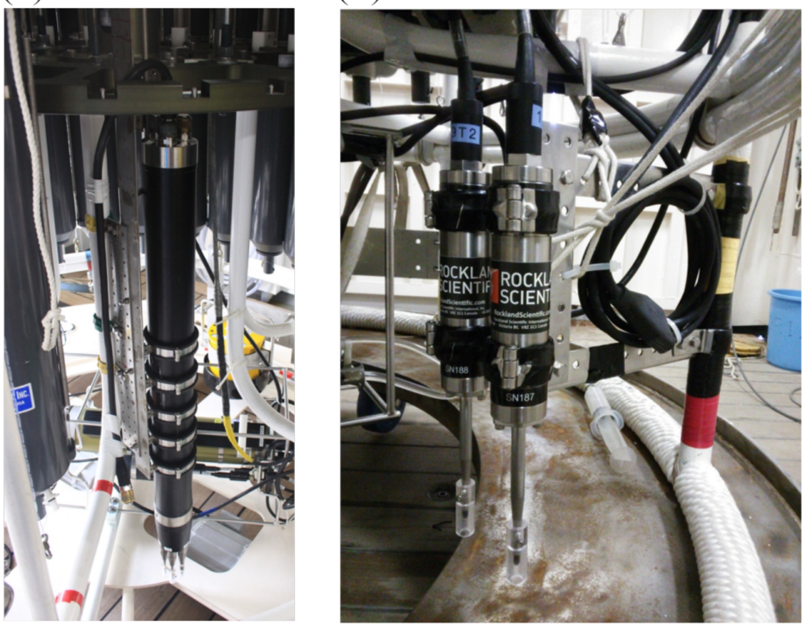

Fig. 3.1. (a) Micro Rider 6000 attached to the CTD-frame during the cruise of KS-15-5 and (b) AFP07 during the cruise of KH-16-3. The probes of FP07 thermistors were set close to the bottom of the frame. ©American Meteorological Society. Used with permission.

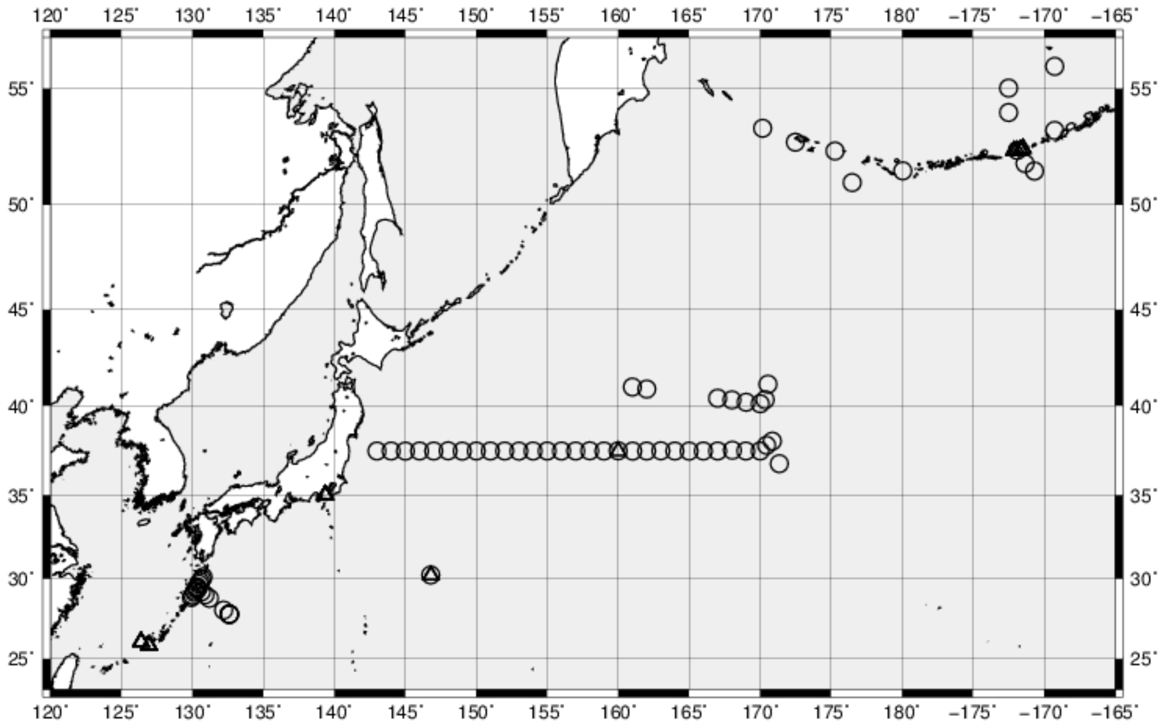

Fig. 3.2. Positions of the 72 stations of the CTD-attached (circles) fast response thermistor measurements (Micro Rider 6000 or AFP07) where free-fall measurements using the vertical microstructure profiler 2000 (VMP) were also performed within 2 hours from the CTD casts. Triangles denote the stations where the repeat casts of the free-fall VMP were performed within 2 hours to examine the temporal variability in the appendix. ©American Meteorological Society. Used with permission.

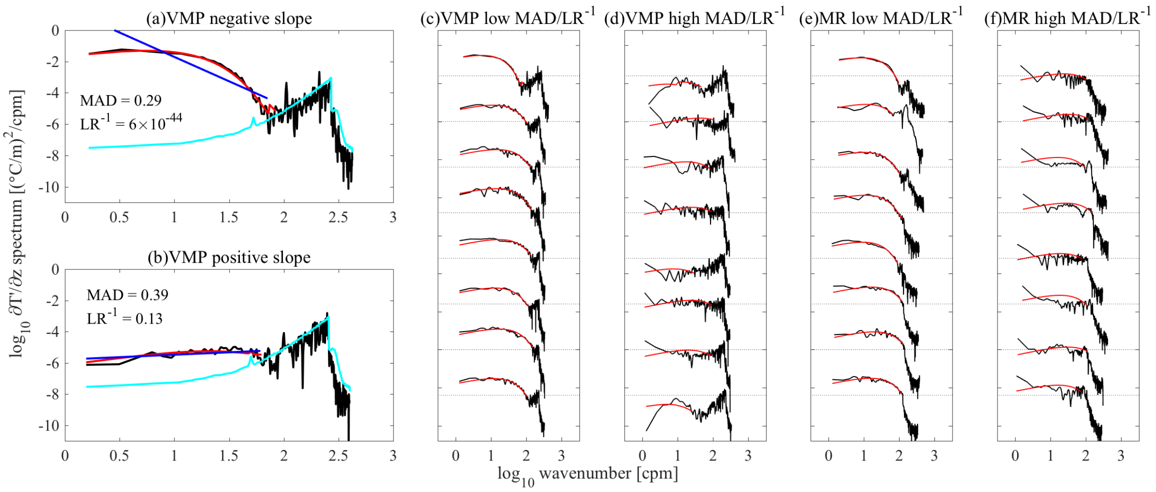

Fig. 3.3. Examples of observed (black) and fitted (red) Kraichnan temperature gradient spectra of free-fall VMP (a - d) and CTD-attached MR (e, f) from the 1-sec-bins. (a) and (b) are examples with noise spectra (light-blue curve) and 1st order power low fit with a (a/b) positive/negative slope of the straight line (blue line). (c) and (e) are examples of well fitted spectra with low maximum absolute deviation MAD (< 0.4) and likelihood ratio LR ($\log_{10}\mathrm{LR}^{-1} < -20$), and (d) and (f) are examples of poorly fitted spectra with high MAD (> 2) and LR ($\log_{10}\mathrm{LR}^{-1} > -2$) to be rejected by the tests. Thin horizontal lines represent $\log_{10}(\partial T'/\partial z)^2 = -4$. All spectra are corrected from the minimum frequency to the cut-off frequency by the frequency response function $\left\{1+(2\pi f\tau_0)^2\right\}^2$, where the 1/4 attenuation time constant $\tau_0 = 3$ msec. ©American Meteorological Society. Used with permission.

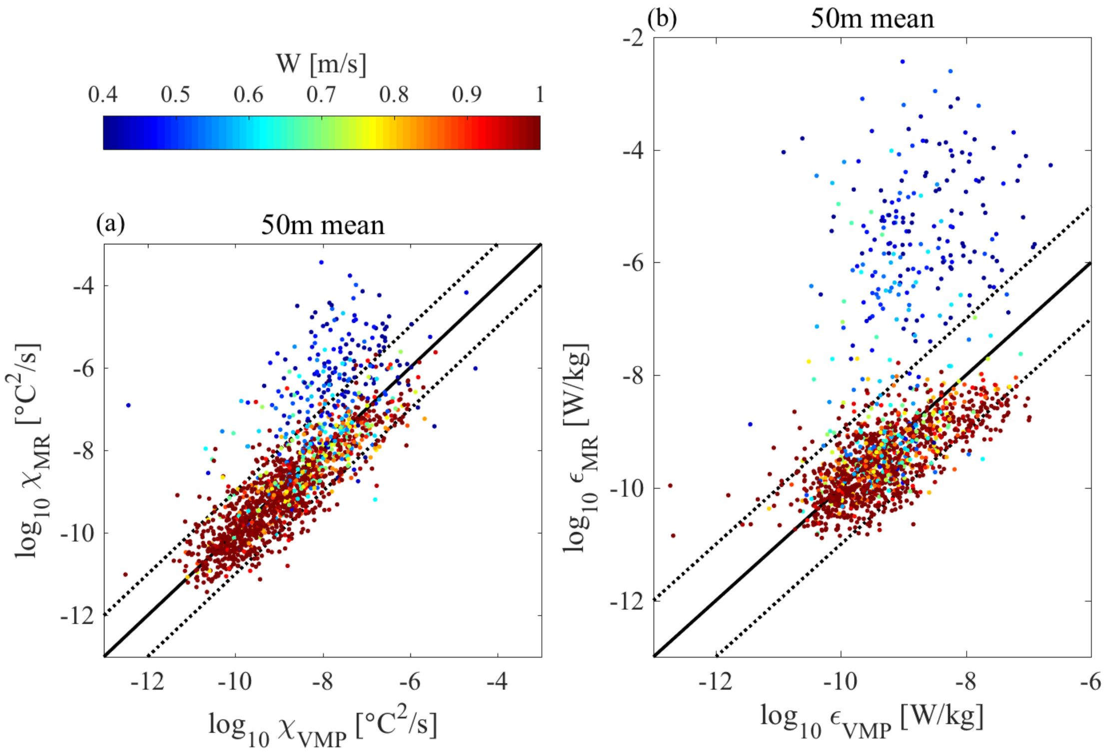

Fig. 3.4. Comparison of 50-m-mean χ (a) and ε (b) from VMP (horizontal axis) and MR (vertical axis). Color of dots denote the fall rate W of MR. Solid and dotted black lines denote $y = x$ and $y = 10^{\pm 1}x$, respectively. ©American Meteorological Society. Used with permission.

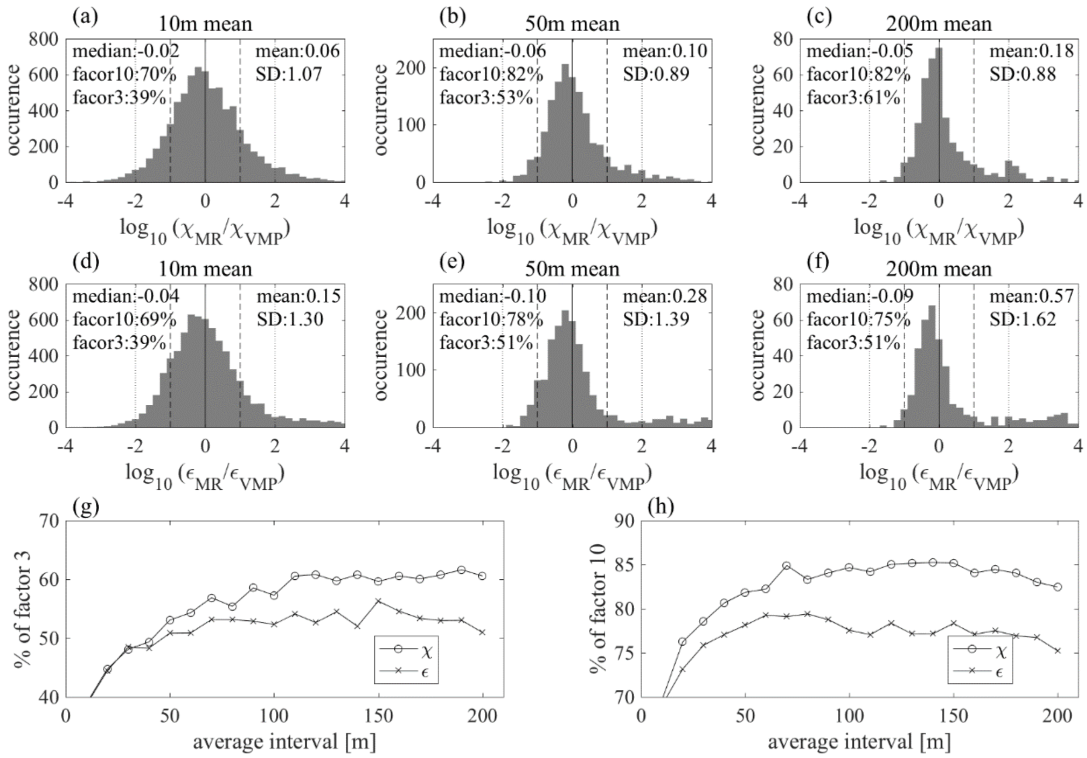

Fig. 3.5. Histograms of $\log_{10}(\chi_{MR}/\chi_{VMP})$ (a-c) and $\log_{10}(\varepsilon_{MR}/\varepsilon_{VMP})$ (d-f) for 10 m-mean (a, d), 50 m-mean (b, e), and 200 m-mean (c, f). The "median", "mean", and "SD" of the figures are the median, arithmetic mean, and standard deviation of $\log_{10}\{\chi_{MR}/\chi_{VMP}(\varepsilon_{MR}/\varepsilon_{VMP})\}$. "factor10", and "factor3" are the percentage of data within factors of 10, and 3, respectively. (g, h) Dependence of ratios (in %) of data within factors of 3 (g) and 10 (h) on the averaging depth intervals from 10 m to 200 m. Averaging was performed after PF14 tests (MAD < 2, LR > 100, and SNR > 1.5). The vertical solid, dashed, and dotted black lines in (a)-(f) are $x = 1$, factor 10, and factor 100, respectively. ©American Meteorological Society. Used with permission.

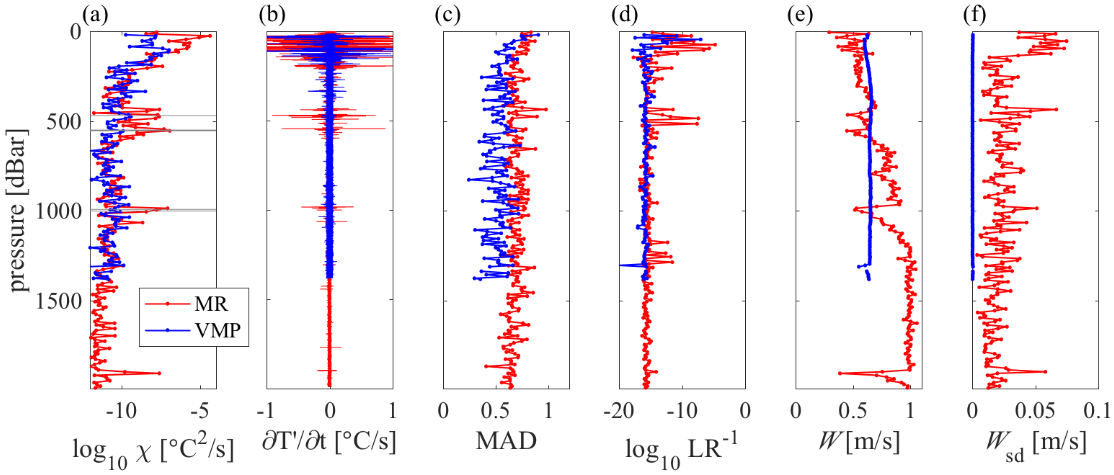

Fig. 3.6. Comparison between CTD-attached MR (red) and free-fall VMP (blue) of the vertical profiles of χ (a), temporal variability of micro-temperature $\partial T'/\partial t$ (b), mean MAD (c), LR^{-1} (d), fall rate W ms^{-1} (e), and standard deviation W_{sd} ms^{-1} (f) of W at Sta.052 observed near the Aleutian Islands (54°59.72N, 172°29.96W). The data in (a) and (c)-(f) were computed from 1-sec bin and then averaged over 10 m after PF14 tests. The data in (b) is raw data sampled at 512 Hz. Temperature gradient spectra at depths with the gray shades in (a) are shown in Fig. 3.7e. ©American Meteorological Society. Used with permission.

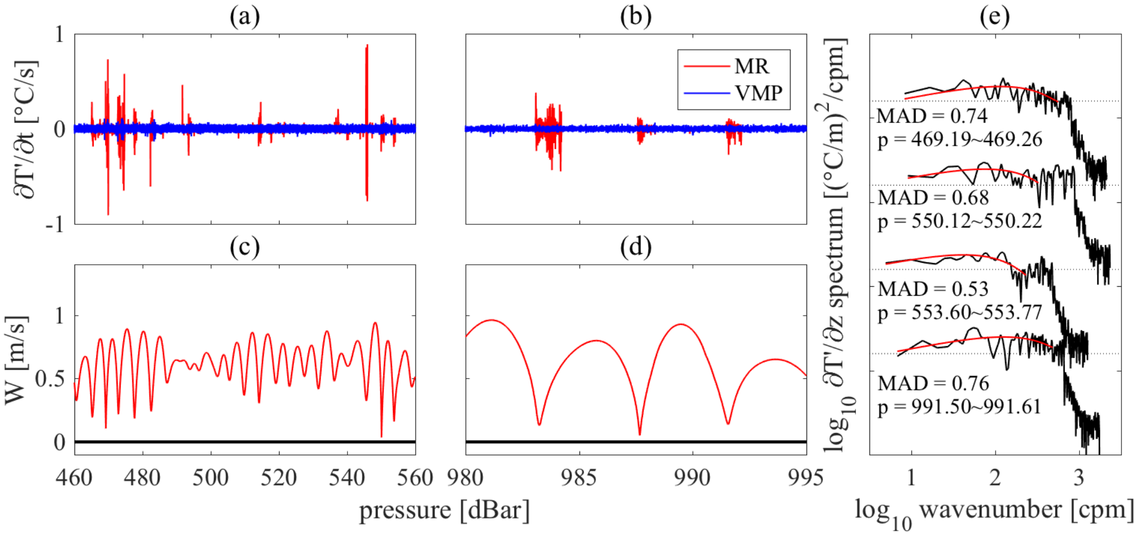

Fig. 3.7. Enlarged view of the raw data of micro-temperature (a, b) and fall rate (c, d) at Sta.052, where the fall rate W is computed from raw 64 Hz pressure data. The horizontal thick lines denote $W = 0$. (e) Examples of temperature gradient spectra at the gray shades of Fig. 3.6a. “p” is the range of pressure over which each spectrum is calculated. ©American Meteorological Society. Used with permission.

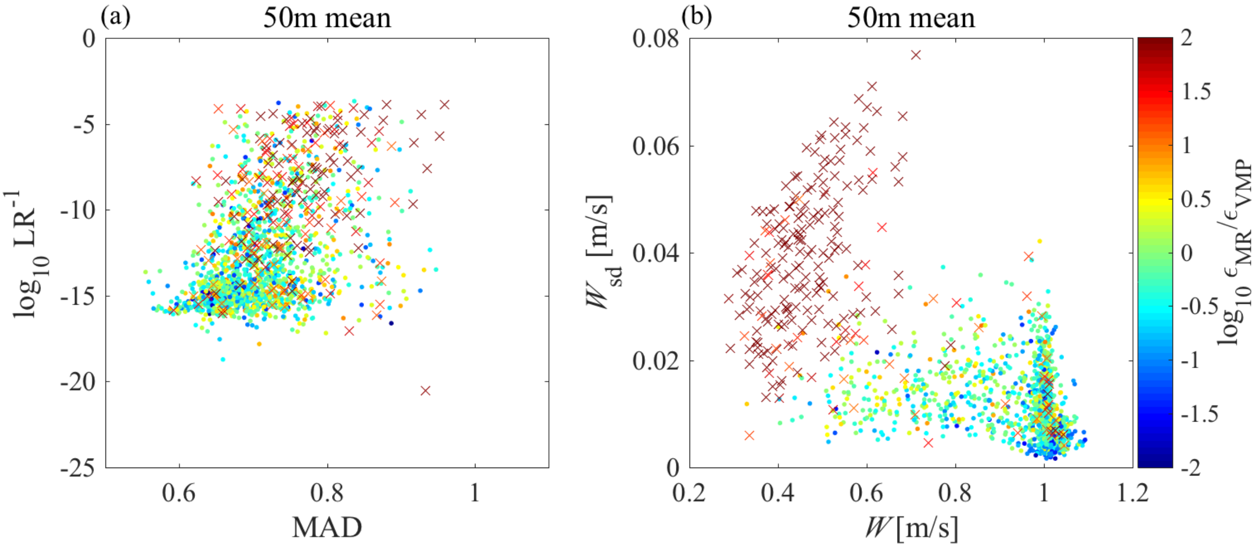

Fig. 3.8. Scatter plots of $\log_{10}(\varepsilon_{MR}/\varepsilon_{VMP})$ represented by color shades for MAD and LR^{-1}(a), and for W and W_{sd} (b) for the 50-m averaged MR dataset after PF14 tests. Crosses denote the overestimated data of $\varepsilon_{MR}/\varepsilon_{VMP}$>10, and dots the data with $\log_{10}(\varepsilon_{MR}/\varepsilon_{VMP})$ <10.

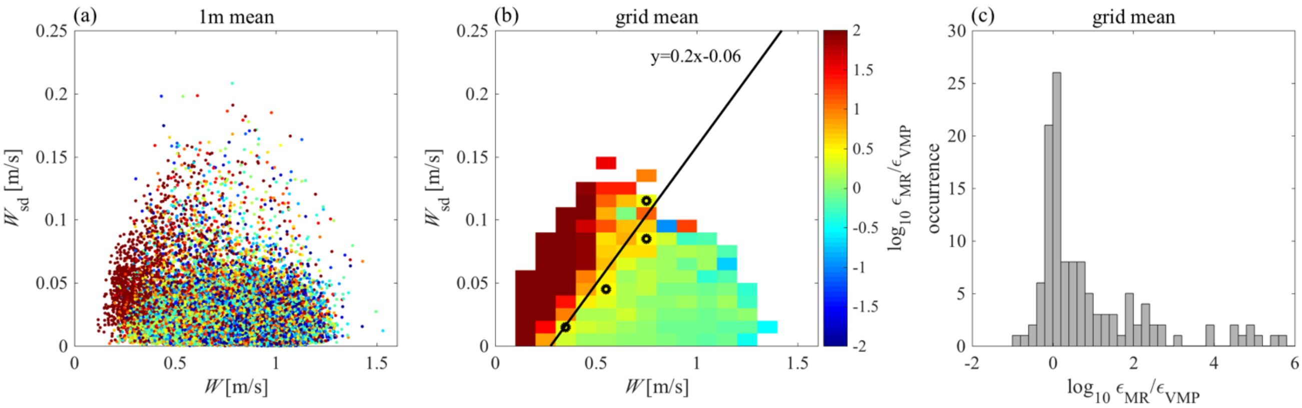

Fig. 3.9. (a) $\log_{10}(\varepsilon_{MR}/\varepsilon_{VMP})$ represented by color shades for W and W_{sd} based on the 1-m averaged MR data after PF14 tests. (b) Geometric mean distribution of $\varepsilon_{MR}/\varepsilon_{VMP}$ of (a) over the grids of $\Delta x \times \Delta y = 0.1 \times 0.01$ ms^{-1}. (c) Histogram of the $\log_{10}(\varepsilon_{MR}/\varepsilon_{VMP})$ data in (b). The circles in (b) are the data with $0.4 < \log_{10}(\varepsilon_{MR}/\varepsilon_{VMP}) < 0.5$, and the solid line (y = 0.2x – 0.06) is the regression for the circles. ©American Meteorological Society. Used with permission.

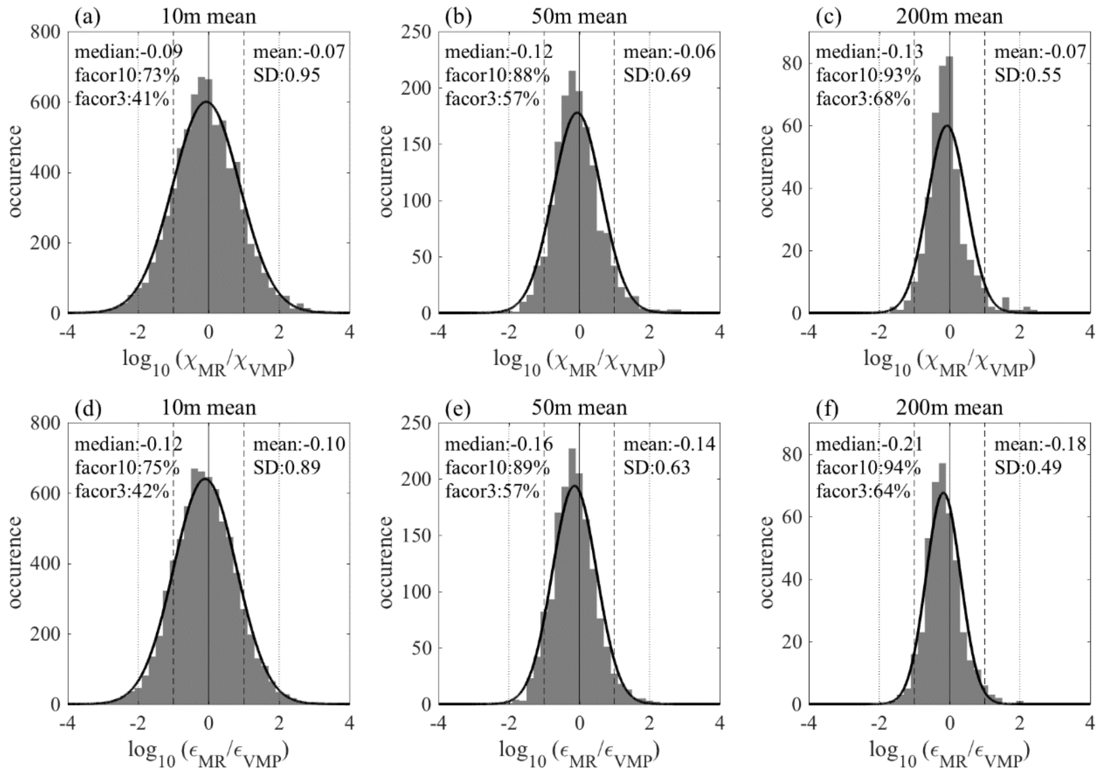

Fig. 3.10. The same as Fig. 3.4a-f but for the data after screening overestimated data with the criteria of $W_{sd} > 0.2W$-0.06. Averaging was performed after eliminating data which satisfy $W_{sd} > 0.2W$-0.06, in addition to PF14 tests. The thick curves are the normal distribution for the "mean" and the "SD". The vertical solid, dashed, and dotted black lines are x=1, factor 10, and factor 100, respectively. ©American Meteorological Society. Used with permission.

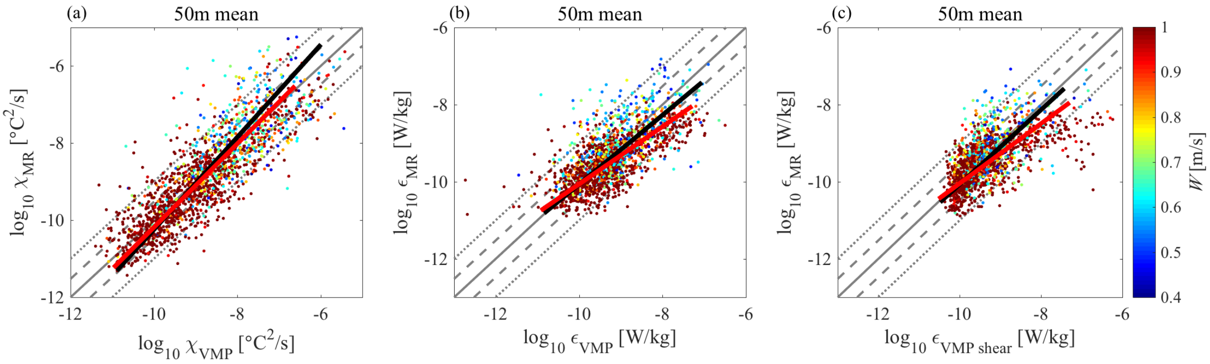

Fig. 3.11. Comparison of 50 m-mean χ (a) and ε (b, c) between from VMP and MR after screening the data using the criteria of PF14 tests for bad spectra and $W_{sd} > 0.2W$-0.06 for overestimated data. In (c), the turbulent energy dissipation rate ε from VMP (horizontal axis) is derived from the shear probes which are the standard sensors for ε. The red and black lines show the 1st order approximation line using principal component analysis in the range of 10^{-11} to 10^{-7}. The red lines are drawn for only $W > 0.9$ ms^{-1}. The solid, broken, and dotted black lines denote $y = x$, $y = 3^{\pm 1}x$ and $y = 10^{\pm 1}x$, respectively. ©American Meteorological Society. Used with permission.

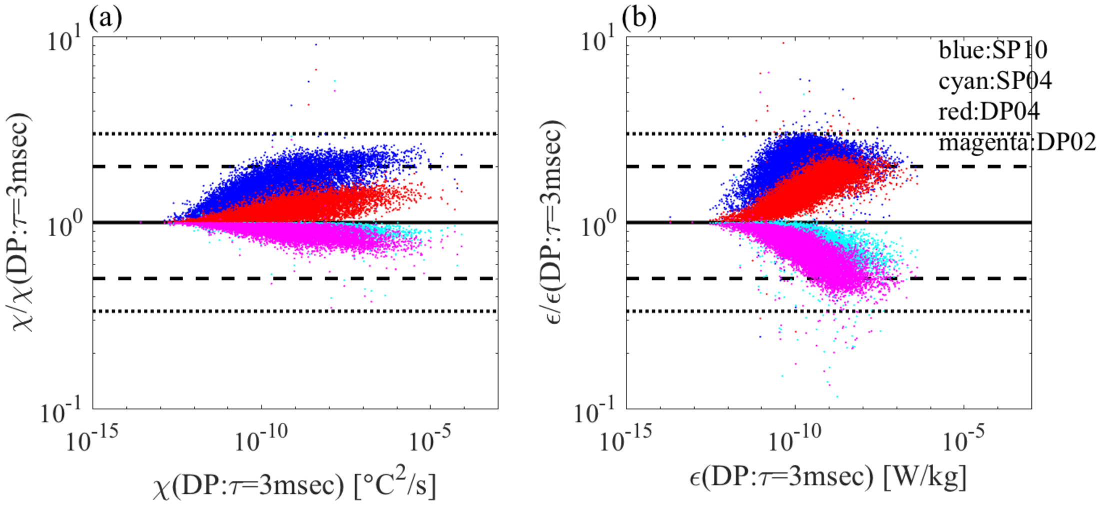

Fig. 3.12. The dependence of the ratios of χ/χ (DP: τ_0 = 3 msec) (a) and ε/ε (DP: τ_0 = 3 msec) (b) on turbulence intensity in the standard double-pole τ_0 = 3 msec case. For the two frequency response functions and time constants τ (Blue: SP10: single-pole τ = 10 msec, cyan: SP04: single-pole τ_0 = 4 msec, red: DP04: double-pole τ = 4 msec, magenta: DP02: double-pole τ_0 = 2 msec). Solid, dashed, and dotted black lines are $y = x$, $y = 2^{\pm 1}x$, and $y = 3^{\pm 1}x$, respectively. ©American Meteorological Society. Used with permission.

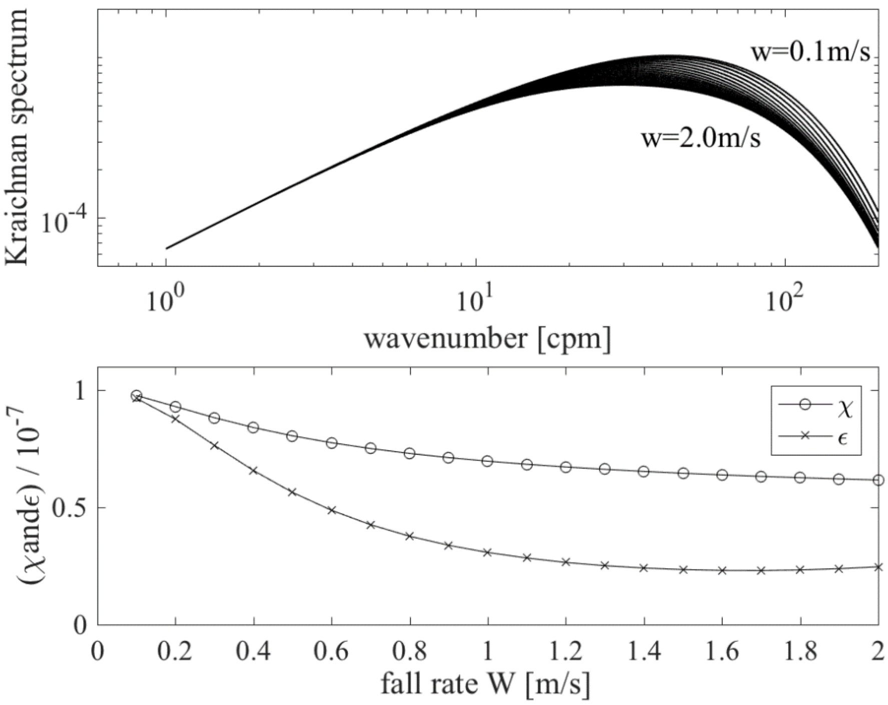

Fig. 3.13. Possible influence of insufficient correction and variable fall rate, *W,* on the spectra (a) and reduction rates (b) of ε and χ for the situation where relatively strong turbulence of $\chi = 10^{-7}$ °C^{2}s^{-1} and $\varepsilon = 10^{-7}$ Wkg^{-1} is measured using a thermistor with the 1/4 time constant τ_0 = 3.5 msec, and is then insufficiently corrected with the faster time constant τ_0 = 3 msec under the variable fall rates from 0.2 to 2 ms^{-1}. ©American Meteorological Society. Used with permission.

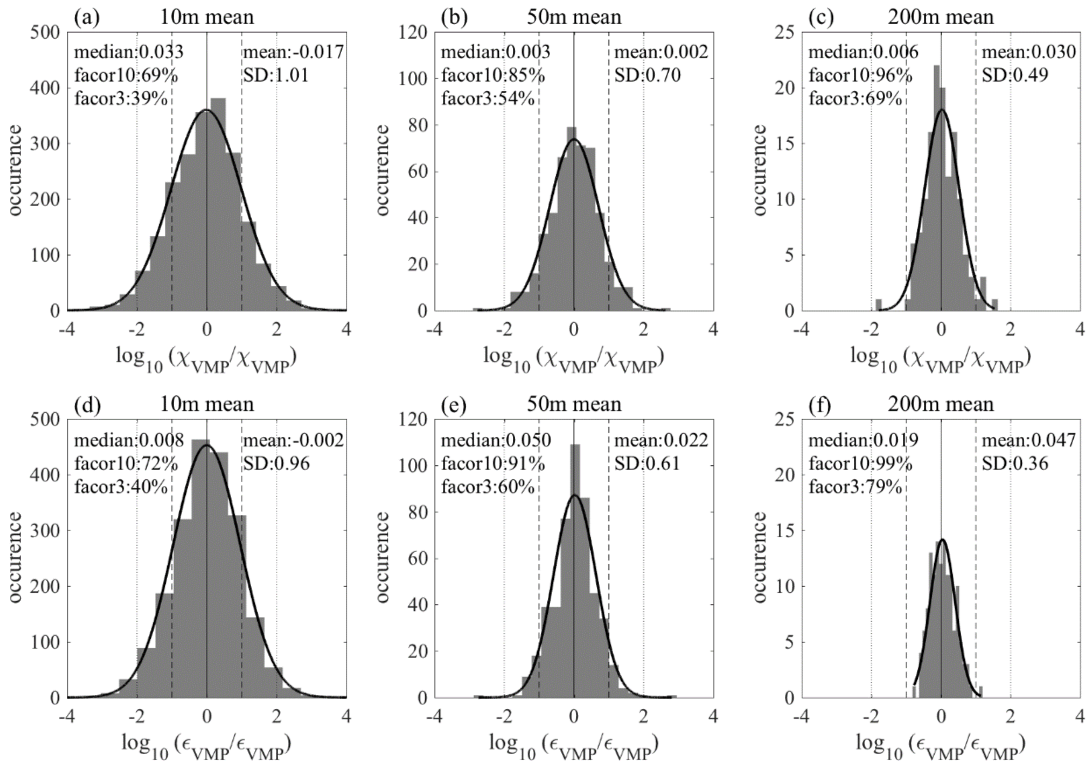

Fig. B1. Distributions of the ratios of VMPs deployed at the same location within intervals of 0.2 ~ 2.9 hours. Forty-five VMP observations were performed, and 32 pairs of profiles at the same location within about 2 hours are compared (triangles in Fig. 3.2). χ and ε were estimated using FP07 thermistors in the same method described in section 2. The legends are the same as those in Fig. 3.10. The thick black curves are normal distributions derived from "mean" and "SD". The vertical solid, dashed, and dotted black lines are x = 1, factor 10, and factor 100, respectively. ©American Meteorological Society. Used with permission.

Chapter 4

Application of the CTD-attached thermistor measurements to basin-scale turbulence distribution in the western North Pacific

第４章については、５年以内に雑誌等で刊行予定のため、非公開

Chapter 5

General conclusion and discussion

5.1 Summary of this thesis

A new observational system, microstructure measurements using the CTD-attached FP07 thermistors, was developed in this thesis in order to widely and frequently perform microstructure observations and then to reveal basin-scale turbulence distributions. Since turbulence estimation with thermistors have not been common due to their insufficient temporal response, assessment of availability was undertaken by comparing energy dissipation rate ε_T from FP07 thermistors with ε_S from shear probe where both the thermistors and shear probes were attached to the same free-fall profiler (Chapter 2). ε_T tended to be less than ε_S as ε_S becomes larger in the case without correction for temperature gradient spectra. By correcting the spectra using the single- or double-pole low-pass filter functions with the time constant of 7 msec (single-pole) or 3 msec (double-pole), respectively, ε_T became consistent with ε_S within a factor of 3 in the range of $10^{-10} < \varepsilon_S < 10^{-7}$ Wkg^{-1}. From the result, fast-response thermistor measurement is concluded to be practical if temperature gradient spectra are appropriately corrected.

Next, influences of "not-free-fall" measurements, that is, variable fall rates of CTD frames were assessed in order to make clear the availability of the CTD-attached measurements (Chapter 3). Comparison of turbulence intensities from this method and free-fall profilers at the same depth and location but with temporal difference within 2 hours show generally good agreement. However, anomalously overestimated data, deviating from a log-normal distribution, appear sporadically in the CTD-attached measurements. They often occurred when the fall rate W was small and its standard deviation W_{sd}, was large. These overestimated outliers could be efficiently removed by rejecting data with the criteria of $W_{sd} > 0.2\ W - 0.06$ computed for a 1 sec interval. After this data screening, thermal and energy dissipation, χ and ε, from CTD-attached and free-fall profilers were consistent within a factor of 3 in the ranges of $10^{-10} < \chi < 10^{-7}$ °C^{2}s^{-1} and $10^{-10} < \varepsilon_T < 10^{-8}$ Wkg^{-1} for 50 m depth-averaged data.

A method to efficiently estimate ε_T was developed. For universal use, key points as below should be followed to reproduce our results.

1) Setting of probes: FP07 thermistors are attached as close to the bottom of the frame as possible, and away from other instruments such as CTD and LADCP as far as possible, as in Fig. 3.1.

2) The bin size: Use 1-second-segmented data to calculate one temperature gradient spectrum, dissipation rate, W, and W_{sd}. The criterion $W_{sd} > 0.2\ W - 0.06$ would be altered if we use greater segment length.

3) Calibration: Each FP07 probe should be calibrated, since there are differences in the time constant between individual probes (Figs. 2.5cd). If calibration is not performed, the error with a factor of 3 should be included after correcting data with the double-pole low-pass filter function with the time constant of 3 msec (Fig. 2.5ab).

Based on the above method of correction and data rejection, basin-scale distributions of turbulence intensity in the deep northwestern Pacific were shown for the first time by microstructure measurements, further by rejecting data at which W takes local minimum (Chapter 4). Turbulence is intensified over rough topography at around seamounts and ridges in regions with strong internal tide. This estimation was confirmed to be consistent (within a factor of 3) with the previous method based on fine-scale O(10~100m) density and velocity. Observed ε_{T} from CTD-attached thermistors depended on internal tide energy and squared buoyancy frequency N^2 ($\propto$ vertical density gradient) through comparing with $\varepsilon_{\mathrm{MODEL}}$ used in a previous ocean general circulation model (OGCM) which reproduced deep Pacific water-masses fields. $\varepsilon_{\mathrm{MODEL}}$ was much larger than the observed ε_{T} by more than 10 times, although spatial variability was correlated between ε_{T} and $\varepsilon_{\mathrm{MODEL}}$. This difference was relaxed to be within a factor of 3 by changing the vertical structure of $\varepsilon_{\mathrm{MODEL}}$ far from internal tide generation sites to be proportional to N^2 and the background constant vertical diffusivity to be the observed minimum of 10^{-7} $\mathrm{m^2s^{-1}}$.

5.2 Remaining issues

5.2.1 Upper and lower limit of ε_{T} measurements

In this thesis, thermistor-derived turbulent energy dissipation rate ε_{T} was confirmed to be available (within a factor of 3) in the range of $10^{-10} < \varepsilon_{\mathrm{S}} < 10^{-7}$ $\mathrm{Wkg^{-1}}$ for free-fall measurements with the fall-rate W = 0.6 - 0.7 $\mathrm{ms^{-1}}$ and in the range of $10^{-10} < \varepsilon_{\mathrm{T}} < 10^{-8}$ $\mathrm{Wkg^{-1}}$ for the CTD-attached measurements with W = 1 $\mathrm{ms^{-1}}$. Availability is not confirmed in the weak turbulence range of $\varepsilon < 10^{-10}$ for all the microstructure measurements including shear probes, free-fall thermistor measurements and the CTD-attached thermistor measurements. Availability in the strong turbulence range of $\varepsilon > 10^{-8}$ $\mathrm{Wkg^{-1}}$ for CTD-attached thermistor measurements and of $\varepsilon > 10^{-7}$ $\mathrm{Wkg^{-1}}$ for free-fall thermistor measurements also remains to be established.

Although weak turbulence regions with $\varepsilon < 10^{-10}$ Wkg^{-1} may be less contributable to the overturning circulation, they cannot be ignored since regions with $\varepsilon < 10^{-10}$ Wkg^{-1} ioccupy most parts of the interior oceans (80 % of the northwestern Pacific as shown in Chapter 4; Gregg 1999). In the range of $\varepsilon_T < 10^{-10}$ Wkg^{-1}, thermistor-based ε_T is generally order of magnitude less than ε_S from shear probes whose detection limit $\varepsilon_S \sim 10^{-10}$ Wkg^{-1} for the 2m-long VMP2000 profiler. To extend the lower limit of microstructure measurements, ε_T needs to be compared with the one from shear probes by using longer and stable microstructure instruments such as VMP5500.

Furthermore, anisotropy needs to be considered in the weak turbulence range. At low buoyancy Reynolds number, assumption of isotropy under which theories of Batchelor / Kraichnan for yielding universal temperature spectrum are established, may not be satisfied because vertical microstructure measurements supply data only in the vertical direction. It may be assessed using glider microstructure measurements which observe both the vertical and horizontal directions together with direct numerical simulations by evaluating micro-temperature and -velocity in 3dimensional fields.

There remains uncertainty also in the strong turbulent range of $\varepsilon > 10^{-8}$ Wkg^{-1} for the CTD-attached thermistor measurements. As discussed in Chapter 3.4, uncertainty in the large ε_T is expected to be more significant for larger W. The upper limit of measurable ε_T, which could depend on W, should be quantified by comparing shear probes and thermistors attached to a free-fall profiler for variable fall speeds.

5.2.2 Data qualification methods

The nucleus points of assessment of the CTD-attached thermistor are 1) calibration of each probe by comparing it with a shear probe and 2) removing abnormal data using fall rate profiles. In this subsection, further improvements of these methods are noted.

In terms of correcting temperature gradient spectra, the best correction function can be determined also in a laboratory experiment by moving sensors in a water tank. Although laboratory experiments were done (e.g. Lueck et al., 1977), they are not conducted in the present day since it is too costly for calibrating many probes (Gregg 1999). However, it should be restarted because thermistors will be used widely in future.

In terms of the data rejection using fall rate, it should be noted again that data rejection criteria developed in Chapter 3 might not be universal as discussed in Chapter 3.4.2. If the CTD-attached thermistors are widely performed in several ships and several institutes by many researchers, the ways of dealing with the sensors will be different. Depending on sensor location, frame size, ship size and winch configuration, the data-rejection threshold of $W_{sd} > 0.2W\text{-}0.06$ would not be common. Actually, data of the local minimum of W need to be removed as well as $W_{sd} > 0.2W\text{-}0.06$ in the cruises of R/V Ryofu-maru and R/V Keifu-maru where variability of fall rates were sometimes greater, probably because those vessels perform CTD observations under more severe environment as high waves (Chapter 4). More flexible criterion is desirable to be derived by performing this method in various situations and platforms.

Finally, it is noted that reliability would be lower after criterion tests since good data become scarce, as mentioned in Chapter 4.3.3. For example, relatively many data are removed by $W_{sd} > 0.2W\text{-}0.06$ near the sea surface and close to the sea floor, where the CTD frame goes down slowly. Near the sea surface (usually, depth < 100 m), integrity of the CTD-attached method was confirmed by comparing it with the free-fall profiler

(Chapter 3). Near the sea floor (usually, height from bottom < 100 m), however, there is no data for comparison because the free-fall profiler used in this thesis cannot reach close to the bottom. Since information of the dissipation near the bottom is required to determine the parameters in near-field turbulence structure, the CTD-attached method should be verified in future by comparing with full ocean-depth microstructure profilers near the bottom.

5.3 Future studies by use of CTD-attached thermistor methods

Wider scale observations should be performed in order to reveal the global distribution of turbulence intensity. In this thesis, basin-scale surface to bottom observations revealed that turbulence is generally weak in most part of intermediate and deep interior oceans with turbulent energy dissipation rate $< 10^{-10}$ Wkg^{-1}. Localized strong turbulent regions such as seamounts and ridges might contribute to meridional-diapycnal overturning circulations more significantly. Furthermore, there are also temporal variations with the periods of tides, annual, inter-annual, decadal and bi-decadal time scales. Seasonal variability of turbulence intensity was reported by Whalen et al. (2015) Qiu et al. (2012) and Inoue (2017), Diurnal variations by Yagi and Yasuda (2012), and 18.6 year tidal modulation by Loder and Garrett 1978, Yasuda et al. 2006, and Osafune and Yasuda 2006. Accordingly, repeated observations are necessary to determine the representative turbulence intensity at each station, especially in strong turbulence regions with large amplitude of tides.

Model-based turbulence estimates needs to be also improved. First, the other source of dissipation should be included. In the upper ocean, wind-induced mixing could be enhanced by propagated near-inertial waves (e.g. Inoue), although the dissipation rates in this thesis were compared with only tide-based model. Lee wave-driven mixing caused by geostrophic flows interacting with rough topography is also considered (Melet et al., 2014). Second, parameters used in the existing tide model of turbulence distribution could be variable. For example, parameters in near-field structure have been set at constant values; local dissipation efficiency q and decay height h are 0.33 and 500 m, respectively (e.g. St Laurent et al., 2001). However, they could be dependent on amplitude of tidal flow and horizontal wavenumber of bottom topography (Hibiya et al., 2017). To determine these parameters, much more observational data are necessary in various oceanic situations depending on tidal flow, topography, latitude, and season. The CTD-attached thermistor measurements developed in the present thesis is expected to contribute to resolving the above issues.

Acknowledgements

I would like to express my gratitude to Prof. Ichiro Yasuda for his many valuable suggestions and discussions on the work.

I would like to thank Prof. Toshiyuki Hibiya, Prof. Yujiro Kitade, Associate Prof. Akira Oka, and Associate Prof. Keita Iga for reviewing the thesis.

I am grateful to the very helpful members of the Atmosphere and Ocean Research Institute, the University of Tokyo. Special thanks to Prof. Hiroshi Niino, Associate Prof. Eitaro Oka, Associate Prof. Shinzo Fujio, Assistant Prof. Daigo Yanagimoto for their helpful suggestions and encouragement.

I also express sincere appreciation to Dr. Maki Nagasawa for variable suggestions and discussions as a co-author of the published articles.

Thanks are extended to the captain, officers, and crew of the R/V Hakuho-maru, the R/V Shinsei-maru, the R/V Multanovskiy, the R/V Ryofu-maru, and the R/V Keifu-maru, in which I participated; KH-13-3, KS-13-T4, KH-13-7, Mu14, KH-15-1, KS-15-5, KS-15-11, KS1508, RF1509, KS-16-3, KH-16-3, KS-16-10, KS-16-12, and KH-17-5.

References

Antonia, R. A., & Orlandi, P. (2003). On the Batchelor constant in decaying isotropic turbulence. Physics of Fluids, 15(7), 2084-2086.

Batchelor, G. K. (1959). Small-scale variation of convected quantities like temperature in turbulent fluid Part 1. General discussion and the case of small conductivity. Journal of Fluid Mechanics, 5(1), 113-133.

Bogucki, D., Domaradzki, J. A., & Yeung, P. K. (1997). Direct numerical simulations of passive scalars with Pr> 1 advected by turbulent flow. Journal of Fluid Mechanics, 343, 111-130.

Bogucki, D. J., Luo, H., & Domaradzki, J. A. (2012). Experimental evidence of the Kraichnan scalar spectrum at high reynolds numbers. Journal of Physical Oceanography, 42(10), 1717-1728.

Corrsin, S. (1964). Further generalization of Onsager's cascade model for turbulent spectra. The Physics of Fluids, 7(8), 1156-1159.

D'Asaro, E. A. (1985). The energy flux from the wind to near-inertial motions in the surface mixed layer. Journal of Physical Oceanography, 15(8), 1043-1059.

Fofonoff, N. P., Hayes, S. P., & Millard, R. C. (1974). WHOI/Brown CTD microprofiler: methods of calibration and data handling. Woods Hole Oceanographic Institution.

Gargett, A. E., Osborn, T. R., & Nasmyth, P. W. (1984). Local isotropy and the decay of turbulence in a stratified fluid. Journal of Fluid Mechanics, 144, 231-280.

Gargett, A. E. (1985). Evolution of scalar spectra with the decay of turbulence in a stratified fluid. Journal of Fluid Mechanics, 159, 379-407.

Garrett, C., & Munk, W. (1975). Space‐time scales of internal waves: A progress report. Journal of Geophysical Research, 80(3), 291-297.

Godeferd, F. S., & Staquet, C. (2003). Statistical modelling and direct numerical simulations of decaying stably stratified turbulence. Part 2. Large-scale and small-scale anisotropy. Journal of Fluid Mechanics, 486, 115-159.

Gregg, M. C., & Meagher, T. B. (1980). The dynamic response of glass rod thermistors. Journal of Geophysical Research: Oceans, 85(C5), 2779-2786.

Gregg, M. C., & Sanford, T. B. (1988). The dependence of turbulent dissipation on stratification in a diffusively stable thermocline. Journal of Geophysical Research: Oceans, 93(C10), 12381-12392.

Gregg, M. C. (1999). Uncertainties and limitations in measuring ε and χ T. Journal of Atmospheric and Oceanic Technology, 16(11), 1483-1490.

Gregg, M. C., E.A. D'Asaro, and J.J. Riley, 2017: Mixing Coefficients and Mixing Efficiency in the Ocean. *Annu. Rev. Fluid Mech*., in press.

Goto, Y., Yasuda, I., & Nagasawa, M. (2016). Turbulence estimation using fast-response thermistors attached to a free-fall vertical microstructure profiler. Journal of Atmospheric and Oceanic Technology, 33(10), 2065-2078.

Goto, Y., Yasuda, I., & Nagasawa, M. (2017). Comparison of turbulence intensity from CTD-attached and free-fall microstructure profilers. Journal of Atmospheric and Oceanic Technolog., in press.

Henyey, F. S., Wright, J., & Flatté, S. M. (1986). Energy and action flow through the internal wave field: An eikonal approach. Journal of Geophysical Research: Oceans, 91(C7), 8487-8495.

Hasumi, H., Yasuda, I., Tatebe, H., & Kimoto, M. (2008). Pacific bidecadal climate variability regulated by tidal mixing around the Kuril Islands. Geophysical Research Letters, 35(14).

Hibiya, T., Ijichi, T., & Robertson, R. (2017). The impacts of ocean bottom roughness and tidal flow amplitude on abyssal mixing. Journal of Geophysical Research: Oceans.

Hill, K. D. (1987). Observations on the velocity scaling of thermistor dynamic response functions. Review of scientific instruments, 58(7), 1235-1238.

Holmes, R. M., Moum, J. N., & Thomas, L. N. (2016). Evidence for seafloor‐intensified mixing by surface‐generated equatorial waves. Geophysical Research Letters, 43(3), 1202-1210.

Ijichi, T., & Hibiya, T. (2015). Frequency-based correction of finescale parameterization of turbulent dissipation in the deep ocean. Journal of Atmospheric and Oceanic Technology, 32(8), 1526-1535.

Itoh, S., Yasuda, I., Nakatsuka, T., Nishioka, J., & Volkov, Y. N. (2010). Fine‐ and microstructure observations in the Urup Strait, Kuril Islands, during August 2006. Journal of Geophysical Research: Oceans, 115(C8).

Itoh, S., Yasuda, I., Yagi, M., Osafune, S., Kaneko, H., Nishioka, J., ... & Volkov, Y. N. (2011). Strong vertical mixing in the Urup Strait. Geophysical Research Letters, 38(16).

Itoh, S., Tanaka, Y., Osafune, S., Yasuda, I., Yagi, M., Kaneko, H., ... & Volkov, Y. N. (2014). Direct breaking of large-amplitude internal waves in the Urup Strait. Progress in Oceanography, 126, 109-120.

Kaneko, H., Yasuda, I., Komatsu, K., & Itoh, S. (2013). Observations of vertical turbulent nitrate flux across the Kuroshio. Geophysical Research Letters, 40(12), 3123-3127.

Kawasaki, T., & Hasumi, H. (2010). Role of localized mixing around the Kuril Straits in the Pacific thermohaline circulation. Journal of Geophysical Research: Oceans, 115(C11).

Klymak, J. M., Moum, J. N., Nash, J. D., Kunze, E., Girton, J. B., Carter, G. S., ... & Gregg, M. C. (2006). An estimate of tidal energy lost to turbulence at the Hawaiian Ridge. Journal of Physical Oceanography, 36(6), 1148-1164.

Kocsis, O., Prandke, H., Stips, A., Simon, A., & Wüest, A. (1999). Comparison of dissipation of turbulent kinetic energy determined from shear and temperature microstructure. Journal of Marine Systems, 21(1), 67-84.

Kraichnan, R. H. (1968). Small‐scale structure of a scalar field convected by turbulence. The Physics of Fluids, 11(5), 945-953.

Kunze, E., Firing, E., Hummon, J. M., Chereskin, T. K., & Thurnherr, A. M. (2006). Global abyssal mixing inferred from lowered ADCP shear and CTD strain profiles. Journal of Physical Oceanography, 36(8), 1553-1576.

Kunze, E. (2017). Internal-wave-driven mixing: Global geography and budgets. Journal of Physical Oceanography, 47(6), 1325-1345.

Ledwell, J. R., Watson, A. J., & Law, C. S. (1993). Evidence for slow mixing across the pycnocline from an open-ocean tracer-release experiment. Nature, 364(6439), 701-703.

Ledwell, J. R., Watson, A. J., & Law, C. S. (1998). Mixing of a tracer in the pycnocline. Journal of Geophysical Research: Oceans, 103(C10), 21499-21529.

Lueck, R. G., Hertzman, O., & Osborn, T. R. (1977). The spectral response of thermistors. Deep Sea Research, 24(10), 951-970.

Lueck, R. G., Wolk, F., & Yamazaki, H. (2002). Oceanic velocity microstructure measurements in the 20th century. Journal of Oceanography, 58(1), 153-174.

Melet, A., Legg, S., & Hallberg, R. (2016). Climatic impacts of parameterized local and remote tidal mixing. Journal of Climate, 29(10), 3473-3500.

Moum, J. N., & Nash, J. D. (2009). Mixing measurements on an equatorial ocean mooring. Journal of Atmospheric and Oceanic Technology, 26(2), 317-336.

Moum, J. N., Perlin, A., Nash, J. D., & McPhaden, M. J. (2013). Seasonal sea surface cooling in the equatorial Pacific cold tongue controlled by ocean mixing. Nature, 500(7460), 64-67.

Munk, W. H. (1966, August). Abyssal recipes. In Deep Sea Research and Oceanographic Abstracts (Vol. 13, No. 4, pp. 707-730). Elsevier.

Munk, W., & Wunsch, C. (1998). Abyssal recipes II: energetics of tidal and wind mixing. Deep Sea Research Part I: Oceanographic Research Papers, 45(12), 1977-2010.

Nagasawa, M., Hibiya, T., Yokota, K., Tanaka, Y., & Takagi, S. (2007). Microstructure measurements in the mid‐depth waters of the North Pacific. Geophysical research letters, 34(5).

Nash, J. D., Caldwell, D. R., Zelman, M. J., & Moum, J. N. (1999). A thermocouple probe for high-speed temperature measurement in the ocean. Journal of Atmospheric and Oceanic Technology, 16(11), 1474-1482.

Nasmyth, P. W. (1970). Oceanic turbulence (Doctoral dissertation, University of British Columbia).

Nikurashin, M., & Ferrari, R. (2011). Global energy conversion rate from geostrophic flows into internal lee waves in the deep ocean. Geophysical Research Letters, 38(8).

Nishioka, J., Nakatsuka, T., Watanabe, Y. W., Yasuda, I., Kuma, K., Ogawa, H., ... & Wakatsuchi, M. (2013). Intensive mixing along an island chain controls oceanic biogeochemical cycles. Global biogeochemical cycles, 27(3), 920-929.

Nishioka, J., & Obata, H. (2017). Dissolved iron distribution in the western and central subarctic Pacific: HNLC water formation and biogeochemical processes. Limnology and Oceanography.

Niwa, Y., & Hibiya, T. (2011). Estimation of baroclinic tide energy available for deep ocean mixing based on three-dimensional global numerical simulations. Journal of oceanography, 67(4), 493.

Oakey, N. S. (1982). Determination of the rate of dissipation of turbulent energy from simultaneous temperature and velocity shear microstructure measurements. Journal of Physical Oceanography, 12(3), 256-271.

Oka, A., & Niwa, Y. (2013). Pacific deep circulation and ventilation controlled by tidal mixing away from the sea bottom. Nature communications, 4, 2419.

Osborn, T. R., & Cox, C. S. (1972). Oceanic fine structure. Geophysical & Astrophysical Fluid Dynamics, 3(1), 321-345.

Osborn, T. R. (1980). Estimates of the local rate of vertical diffusion from dissipation measurements. Journal of Physical Oceanography, 10(1), 83-89.

Panchev, S., & Kesich, D. (1969). Energy spectrum of isotropic turbulence at large wavenumbers. CR Acad. Bulg. Sci, 22, 627-630.

Perlin, A., & Moum, J. N. (2012). Comparison of thermal variance dissipation rates from moored and profiling instruments at the equator. Journal of Atmospheric and Oceanic Technology, 29(9), 1347-1362.

Peterson, A. K., & Fer, I. (2014). Dissipation measurements using temperature microstructure from an underwater glider. Methods in Oceanography, 10, 44-69.

Roget, E., Lozovatsky, I., Sanchez, X., & Figueroa, M. (2006). Microstructure measurements in natural waters: Methodology and applications. Progress in Oceanography, 70(2), 126-148.

Polzin, K. L., Toole, J. M., & Schmitt, R. W. (1995). Finescale parameterizations of turbulent dissipation. Journal of physical oceanography, 25(3), 306-328.

Polzin, K. L., Toole, J. M., Ledwell, J. R., & Schmitt, R. W. (1997). Spatial variability of turbulent mixing in the abyssal ocean. Science, 276(5309), 93-96.

Ruddick, B., Anis, A., & Thompson, K. (2000). Maximum likelihood spectral fitting: The Batchelor spectrum. Journal of Atmospheric and Oceanic Technology, 17(11), 1541-1555.

Saffman, P. G. (1963). On the fine-scale structure of vector fields convected by a turbulent fluid. Journal of Fluid Mechanics, 16(4), 545-572.

Sanchez, X., Roget, E., Planella, J., & Forcat, F. (2011). Small-scale spectrum of a scalar field in water: the Batchelor and Kraichnan models. Journal of Physical Oceanography, 41(11), 2155-2167.

Shih, L. H., Koseff, J. R., Ivey, G. N., & Ferziger, J. H. (2005). Parameterization of turbulent fluxes and scales using homogeneous sheared stably stratified turbulence simulations. Journal of Fluid Mechanics, 525, 193-214.

St. Laurent, L. C., Toole, J. M., & Schmitt, R. W. (2001). Buoyancy forcing by turbulence above rough topography in the abyssal Brazil Basin. Journal of Physical Oceanography, 31(12), 3476-3495.

St Laurent, L. C., Simmons, H. L., & Jayne, S. R. (2002). Estimating tidally driven mixing in the deep ocean. Geophysical Research Letters, 29(23).

Tanaka, Y., Hibiya, T., & Niwa, Y. (2010). Assessment of the effects of tidal mixing in the Kuril Straits on the formation of the North Pacific Intermediate Water. Journal of Physical Oceanography, 40(12), 2569-2574.

Tanaka, Y., Yasuda, I., Hasumi, H., Tatebe, H., & Osafune, S. (2012). Effects of the 18.6-yr modulation of tidal mixing on the North Pacific bidecadal climate variability in a coupled climate model. Journal of Climate, 25(21), 7625-7642.

Tanaka, Y., Yasuda, I., Osafune, S., Tanaka, T., Nishioka, J., & Volkov, Y. N. (2014). Internal tides and turbulent mixing observed in the Bussol Strait. Progress in Oceanography, 126, 98-108.

Tanaka, T., Yasuda, I., Kuma, K., & Nishioka, J. (2012). Vertical turbulent iron flux sustains the Green Belt along the shelf break in the southeastern Bering Sea. Geophysical Research Letters, 39(8).

Tanaka, T., Yasuda, I., Tanaka, Y., & Carter, G. S. (2013). Numerical study on tidal mixing along the shelf break in the Green Belt in the southeastern Bering Sea. Journal of Geophysical Research: Oceans, 118(12), 6525-6542.

Tanaka, T., Yasuda, I., Onishi, H., Ueno, H., & Masujima, M. (2015). Observations of current and mixing around the shelf break in Pribilof Canyon in the Bering Sea. Journal of oceanography, 71(1), 1-17.

Thorpe, S. A., 2007: An Introduction to Ocean Turbulence. Cambridge University Press, 240pp.

Toole, J. M., Schmitt, R. W., & Polzin, K. L. (1994). Estimates of diapycnal mixing in the abyssal ocean. Science, 264(5162), 1120-1123.

Waterhouse, A. F., MacKinnon, J. A., Nash, J. D., Alford, M. H., Kunze, E., Simmons, H. L., ... & Talley, L. D. (2014). Global patterns of diapycnal mixing from measurements of the turbulent dissipation rate. Journal of Physical Oceanography, 44(7), 1854-1872.

Wijesekera, H., Padman, L., Dillon, T., Levine, M., Paulson, C., & Pinkel, R. (1993). The application of internal-wave dissipation models to a region of strong mixing. Journal of physical oceanography, 23(2), 269-286.

Whalen, C. B., Talley, L. D., & MacKinnon, J. A. (2012). Spatial and temporal variability of global ocean mixing inferred from Argo profiles. Geophysical Research Letters, 39(18).

Whalen, C. B., MacKinnon, J. A., Talley, L. D., & Waterhouse, A. F. (2015). Estimating the mean diapycnal mixing using a finescale strain parameterization. Journal of Physical Oceanography, 45(4), 1174-1188.

Wolk, F., Yamazaki, H., Seuront, L., & Lueck, R. G. (2002). A new free-fall profiler for measuring biophysical microstructure. Journal of Atmospheric and Oceanic Technology, 19(5), 780-793.

Yagi, M., & Yasuda, I. (2012). Deep intense vertical mixing in the Bussol'Strait. Geophysical Research Letters, 39(1).

Yagi, M., & Yasuda, I. (2013). A modified method for estimating vertical profiles of turbulent dissipation rate using density inversions in the Kuril Straits. Journal of oceanography, 69(2), 203-214.

Yagi, M., Yasuda, I., Tanaka, T., Tanaka, Y., Ono, K., Ohshima, K. I., & Katsumata, K. (2014). Re-evaluation of turbulent mixing vertical structure in the Bussol'Strait and its impact on water masses in the Okhotsk Sea and the North Pacific. Progress in Oceanography, 126, 121-134.

Yamazaki, H., & Osborn, T. (1990). Dissipation estimates for stratified turbulence. Journal of Geophysical Research: Oceans, 95(C6), 9739-9744.